View metadata, citation and similar papers at core.ac.uk

brought to you by CORE

provided by University of Queensland eSpace

The Astronomical Journal, 133:1722–1740, 2007 April

© 2007. The American Astronomical Society. All rights reserved. Printed in U.S.A.

INTERNAL PROPERTIES OF ULTRACOMPACT DWARF GALAXIES IN THE VIRGO CLUSTER

E. A. Evstigneeva
Department of Physics, University of Queensland, Brisbane, QLD 4072, Australia; katya@physics.uq.edu.au

M. D. Gregg[1]
Department of Physics, University of California, Davis, CA 95616, USA; gregg@igpp.ucllnl.org

M. J. Drinkwater
Department of Physics, University of Queensland, Brisbane, QLD 4072, Australia; m.drinkwater@uq.edu.au

and

M. Hilker[2]
Argelander-Institut für Astronomie, Universität Bonn, 53121 Bonn, Germany; mhilker@eso.org

Received 2006 August 9; accepted 2006 December 14

ABSTRACT

We present new imaging and spectroscopic observations of six ultracompact dwarf (UCD) galaxies in the Virgo Cluster, along with reanalyzed data for five Fornax Cluster UCDs. These are the most luminous UCDs: -14 mag $< M_V < -12$ mag. Our *Hubble Space Telescope* imaging shows that most of the UCDs have shallow or steep cusps in their cores; only one UCD has a flat "King" core. None of the UCDs show tidal cutoffs down to our limiting surface brightness. Spectroscopic analysis shows that Virgo UCDs are old (older than 8 Gyr) and have metallicities in the range from $[Z/H] = -1.35$ to +0.35 dex. Five Virgo UCDs have supersolar $[\alpha/Fe]$ abundance ratios, and one Virgo UCD has a solar abundance ratio. The supersolar $[\alpha/Fe]$ abundances are typical of old stellar populations found in globular clusters and elliptical galaxies. We find that Virgo UCDs have structural and dynamical properties similar to Fornax UCDs. The Virgo and Fornax UCDs all have masses $\approx(2–9)\times10^7\ M_\odot$ and mass-to-light ratios $\approx(3–5)\ M_\odot/L_{\odot,V}$. The dynamical mass-to-light ratios for Virgo UCDs are consistent with simple stellar population model predictions: the Virgo UCDs do not require dark matter to explain their mass-to-light ratios. We conclude that the internal properties of Virgo UCDs are consistent with them being the high-mass/high-luminosity extreme of known globular cluster populations. We refrain from any firm conclusions on Fornax UCD origins until accurate age, metallicity, and α-abundance estimates are obtained for them. Some of our results, notably the fundamental plane projections, are consistent with the formation of UCDs by the simple removal of the halo from the nuclei of nucleated dwarf galaxies. However, the ages, metallicities, and abundances for Virgo UCDs are not consistent with this simple stripping model. It might be consistent with more sophisticated models of the stripping process that include the effects of gas removal on the chemical evolution of the nuclei.

Key words: galaxies: abundances — galaxies: dwarf — galaxies: formation — galaxies: kinematics and dynamics — galaxies: star clusters — galaxies: structure

Online material: color figures

1. INTRODUCTION

Recent spectroscopic surveys of the Fornax and Virgo galaxy clusters have revealed a new class of compact stellar system, ultracompact dwarf galaxies (UCDs) with properties intermediate between the largest globular clusters (GCs) and the smallest dwarf galaxies. The defining properties of the first UCDs found are that they are significantly more luminous than most known GCs ($-14 < M_V < -12$), but they are mostly unresolved in ground-based sky survey images. In this paper we present detailed observations of a new sample of UCDs in the Virgo Cluster in order to test hypotheses for the formation of these objects.

The Fornax Cluster UCD objects were discovered independently in studies of GC systems around the central galaxy NGC 1399 (Minniti et al. 1998; Hilker et al. 1999) and in studies of compact dwarf galaxies in the cluster (Drinkwater et al. 2000; Phillipps et al. 2001). Confirmed UCDs have subsequently been found in the Virgo Cluster (Haşegan et al. 2005; Jones et al. 2006), and UCD candidates have been identified in the more distant cluster Abell 1689 (Mieske et al. 2004). At low luminosities ($M_V > -12$) the distinction between UCDs and GCs is not clear (see discussions in Drinkwater et al. [2004] and Mieske et al. [2006]), but in this paper we focus on the most luminous objects ($-14 < M_V < -12$).

Given their intermediate nature, most formation hypotheses for UCDs relate them to either GCs or dwarf galaxies. They could be highly luminous intracluster GCs (e.g., Mieske et al. 2002). Alternatively, UCDs may result from the tidal disruption of nucleated dwarf elliptical galaxies. This process can leave the nucleus intact on intracluster orbit (Bekki et al. 2001, 2003) as a UCD. Other formation scenarios include UCDs being the evolved products of massive super star clusters formed in galaxy mergers (Fellhauer & Kroupa 2002), or primordial objects (Phillipps et al. 2001).

It is hard to provide definitive observational tests of these different scenarios for UCD formation. This is partly because the various scenarios do not always make very different predictions, but the observational picture also remains far from complete.

[1] Institute for Geophysics and Planetary Physics, Lawrence Livermore National Laboratory, Livermore, CA 94550, USA.

[2] European Southern Observatory, 85748 Garching bei München, Germany.

TABLE 1
SPECTROSCOPY TARGETS

Name	Object type	R.A. (J2000.0)	Decl. (J2000.0)	Exposure Times (s)
Strom 417	M87 GC	12 31 01.29	+12 19 25.6	3×1800
VUCD 1	UCD	12 30 07.61	+12 36 31.1	3×1800
VUCD 3/Strom 547	UCD/M87 GC	12 30 57.40	+12 25 44.8	3×1800
VUCD 4	UCD	12 31 04.51	+11 56 36.8	3×1800
VUCD 5	UCD	12 31 11.90	+12 41 01.2	3×1800
VUCD 6	UCD	12 31 28.41	+12 25 03.3	3×1800
VUCD 7	UCD	12 31 52.93	+12 15 59.5	2×1800
VCC 1407	dE,N	12 32 02.70	+11 53 25.0	$(1\times1800)+(2\times1200)$
NGC 4486B	E	12 30 31.92	+12 29 27.4	1×721

NOTE.—Units of right ascension are hours, minutes, and seconds, and units of declination are degrees, arcminutes, and arcseconds.

The observational tests can broadly be divided into statistical population studies (e.g., the distribution of UCDs compared to other objects) and detailed studies of the internal properties (e.g., internal velocity dispersion) of the UCDs. In this paper we focus on the latter.

Our previous investigations have focused on the Fornax Cluster UCDs. We used *Hubble Space Telescope* (*HST*) imaging and ESO Very Large Telescope spectroscopy to compare the five original UCDs to GCs and nucleated dwarf galaxies (Drinkwater et al. 2003). We concluded that UCDs were distinct from known GC populations, as they followed a different relation between internal velocity dispersion and luminosity. The UCD properties were, however, consistent with the threshing model in which the dwarf galaxy nuclei survived tidal disruption with no significant change to their luminosity or velocity dispersion.

The tidal disruption hypothesis was also supported by Haşegan et al. (2005) in their analysis of 10 compact "dwarf-globular transition objects" found in *HST* images of Virgo Cluster galaxies. The transition objects of Haşegan et al. have slightly lower luminosities ($-12 < M_V < -11$) than the Fornax UCDs, but the brighter ones were found to be significantly different to GCs, both in size and in following galaxy-scaling relations. Haşegan et al. suggest that bona fide UCDs are also distinguished by the presence of dark matter, as some of their objects have $6 < M/L_V < 9$.

A detailed analysis of the stellar populations of compact objects in the Fornax Cluster (Mieske et al. 2006) has reached quite different conclusions. They measured spectroscopic metallicities for 26 compact objects with luminosities spanning both UCDs and GCs and found a break in the distribution at about $M_V = -11$. The more luminous objects have a narrow metallicity distribution with mean $[\mathrm{Fe/H}] = -0.62 \pm 0.05$, whereas the less luminous objects show a much broader range of metallicity and a significantly lower mean (0.56 dex lower). There is a break in the size-luminosity relation for these objects at the same luminosity. Mieske et al. note that the metallicity of the dwarf galaxy nuclei in their sample is significantly lower than that of the UCDs, which, in turn, are better matched by models of massive young star clusters. They therefore suggest that the UCDs in the Fornax Cluster are formed as a result of galaxy mergers, but note that the properties of the Virgo Cluster UCDs are more consistent with the stripping model.

In this paper we present new imaging and spectroscopic observations of the Virgo Cluster UCDs listed by Jones et al. (2006). These are analyzed along with existing data for the luminous Fornax Cluster UCDs (Drinkwater et al. 2003). In § 2 we describe the high-resolution spectroscopic observations, and in § 3 we describe the corresponding *HST* imaging. We present an overview of our results in § 4 by comparing the UCDs with other objects in various projections of the fundamental plane. In § 5 we investigate the UCD dynamics in more detail, calculating their mass-to-light (M/L) ratios, and in § 6 we examine the ages and chemical composition of their stellar populations. Our main results and conclusions are given in § 7. We use distance moduli of 30.92 and 31.39 mag for the Virgo and Fornax Clusters, respectively (Freedman et al. 2001).

2. SPECTROSCOPY

Observations of the six Virgo UCDs, a comparison M87 GC (Strom 417), a comparison dwarf galaxy nucleus (VCC 417), and the NGC 4486B galaxy (its central part) were carried out on 2003 April 6–7 with the Echelle Spectrograph and Imager (ESI) on the Keck II telescope in the echellette mode (Table 1). A slit width of 0.75″ was used, providing an instrumental resolution of $\approx$50 km s^{-1} (FWHM) or $\lambda/\Delta\lambda \approx 6000$. The wavelength range is 3900–11000 Å, distributed over 10 echelle orders, with a dispersion of 11.4 km s^{-1} pixel^{-1}. The exposure times are given in Table 1. In addition, standard stars of spectral types in the range between G8 III and M0 III (Table 2) were observed for use as templates for the radial velocity and velocity dispersion measurements and line index calibrators. The standard stars were observed in two ways: held centered in the slit, and also moving perpendicularly across the slit ("smeared") to simulate the appearance of extended sources that overfill the slit and consequently have

TABLE 2
STELLAR TEMPLATES

Template No.	Template	Spectral Type	[Fe/H]	Reference
1	HD 040460	K1 III	−0.50	1
2	HD 048433	K1 III	−0.26	2
3	HD 137704	K4 III	−0.43	2
4	HD 139195	K0 III	−0.17	2
5	HD 139669	K5 III	−0.13	3
6	HD 141680	G8 III	−0.28	2
7	HD 142574	M0 III	...	...
8	HD 143107	K2 III	−0.32	2
9	HD 145148	K1.5 IV	...	...
10	HD 145675	K0 V	0.31	4
11	HD 147677	K0 III	−0.08	2
12	HD 148513	K4 III	0.04/−0.31	2, 5
13	HD 149161	K4 III	−0.23	2

REFERENCES.—(1) Cottrell & Sneden 1986; (2) McWilliam 1990; (3) Valdes et al. 2004; (4) Peterson 1978; (5) Luck & Challener 1995.

TABLE 3
HELIOCENTRIC LINE-OF-SIGHT VELOCITIES AND VELOCITY DISPERSIONS OBTAINED WITH THE WAVELENGTH RANGE 8400–8750 Å, INCLUDING CaT ABSORPTION LINES

	DIRECT FITTING			CROSS-CORRELATION	
OBJECT	v_{helio} (kms^{-1})	σ (kms^{-1})	Templates	v_{helio} (kms^{-1})	σ (kms^{-1})
VUCD 1	1227.8 ± 1.7	33.8 ± 1.7	6	1225.4 ± 3.7	34.0 ± 1.6
VUCD 3/Strom 547	710.6 ± 3.5	37.7 ± 1.4	2, 8	711.4 ± 3.4	37.8 ± 1.6
VUCD 4	919.7 ± 1.7	23.9 ± 2.2	6	916.5 ± 4.2	21.3 ± 2.2
VUCD 5	1293.1 ± 1.7	27.4 ± 1.7	6	1290.3 ± 3.0	24.9 ± 2.0
VUCD 6	2105.3 ± 1.7	24.6 ± 1.8	6	2101.7 ± 3.9	22.2 ± 2.2
VUCD 7	988.3 ± 2.7	36.7 ± 3.7	6	985.7 ± 5.0	35.6 ± 1.6
Strom 417	1863.5 ± 1.6	26.4 ± 2.1	6	1860.6 ± 3.0	25.8 ± 2.0
VCC 1407	1018.9 ± 3.2	29.3 ± 2.5	1, 2, 3, 4, 6	1019.4 ± 5.7	26.6 ± 2.1
NGC 4486B	1558.4 ± 4.2	211.3 ± 4.8	2, 3, 7, 8, 11, 12	1546.9 ± 32.8	198.1 ± 15.5

NOTES.—In the direct-fitting method, the best-fitting template stars were used to determine velocities and velocity dispersions. The best-fitting templates (as numbered in Table 2) are given in the "Templates" column. The σ and v_{helio} values are the mean values using all observations of the best-fitting template(s). In the cross-correlation method, σ and v_{helio} are the mean values using all stellar templates.

slightly lower spectral resolution. The seeing was a stable 0.8″ the first night, and ranged from 0.8″ to 1.1″ the second. The first night was photometric; the second had occasional light cirrus.

The data were reduced using scripts in IRAF and IDL specifically written to handle the ESI data format and idiosyncrasies, but that otherwise are standard procedures for CCD data. Spectra were extracted over a 1.5″ aperture centered on the peak, taking in nearly all the light from the UCDs and GCs. The relative flux scale was determined using nightly observations of Feige 34. The signal-to-noise ratio (S/N) for each integration ranges from ∼15 to 25 pixel^{-1}, yielding a final S/N of 30–50 after co-adding the multiple observations of each target.

The radial velocity and velocity dispersion of our objects were determined using two different techniques: the direct-fitting method (as described and implemented by van der Marel 1994) and the cross-correlation method (Tonry & Davis 1979; as implemented in RVSAO/IRAF). In the direct-fitting method the template-star spectrum (Table 2) is broadened with Gaussian functions of variable σ in velocity space. The resulting set of spectra are then compared with the object spectrum. The best-fitting Gaussian function is determined by χ^2 minimization in pixel space. The second method is to cross-correlate the object spectrum with the stellar template spectrum to determine the width of the cross-correlation peak and the redshift. The correlation width is used to estimate the velocity dispersion by comparison with results from artificially broadening the template stars by convolution with Gaussian functions of known width. This method is less sensitive to the exact match between template and object spectra than the direct-fitting method.

Velocities and velocity dispersions were obtained from the CaT (8400–8750 Å) and Mg *b* (5100–5250 Å) regions. The measured values are given in Tables 3 and 4 and are consistent, within the measurement errors, for the two techniques and the two wavelength regions. The exception is VUCD 3. In the following discussion we use values obtained as the mean of the two wavelength regions and use the direct-fitting method, as it gives smaller measurement errors. The adopted velocities and velocity dispersions for the observed objects are shown in Table 5. Our measurements for NGC 4486B are in good agreement with Bender et al. (1992). There were almost no differences in the velocity and velocity dispersion measurements obtained with smeared and unsmeared stellar templates.

The two wavelength regions give significantly different velocity dispersions for VUCD 3: ≈49 km s^{-1} for the Mg *b* region, but only ≈38 km s^{-1} for the CaT region. This discrepancy appears to be real. We suspect this may be because the ratio of giant to dwarf

TABLE 4
HELIOCENTRIC LINE-OF-SIGHT VELOCITIES AND VELOCITY DISPERSIONS OBTAINED WITH THE WAVELENGTH RANGE 5100–5250 Å INCLUDING Mg *b* ABSORPTION LINES

	DIRECT FITTING			CROSS CORRELATION	
OBJECT	v_{helio} (kms^{-1})	σ (kms^{-1})	Templates	v_{helio} (kms^{-1})	σ (kms^{-1})
VUCD 1	1219.5 ± 1.3	34.4 ± 1.6	2	1225.1 ± 9.3	32.8 ± 6.1
VUCD 3/Strom 547	716.4 ± 1.2	46.5 ± 1.6	9	717.4 ± 12.7	51.4 ± 4.7
VUCD 4	912.5 ± 1.5	23.9 ± 1.8	2	916.8 ± 5.8	15.7 ± 8.3
VUCD 5	1285.8 ± 1.0	28.9 ± 1.5	2	1291.8 ± 6.3	26.0 ± 6.8
VUCD 6	2096.7 ± 1.4	25.7 ± 1.8	2	2103.1 ± 6.8	20.4 ± 7.6
VUCD 7	980.7 ± 3.5	39.2 ± 4.4	2	986.6 ± 7.7	33.3 ± 6.0
Strom 417	1857.1 ± 1.4	28.8 ± 1.6	2	1863.4 ± 6.7	25.1 ± 6.9
VCC 1407	1018.8 ± 3.3	31.4 ± 2.7	1, 2, 6, 11	1020.2 ± 7.5	28.5 ± 6.5
NGC 4486B	1556.3 ± 8.7	199.1 ± 5.0	2, 6, 8, 9	1558.7 ± 52.1	230.4 ± 26.3

NOTES.—In the direct-fitting method, the best-fitting template stars were used to determine velocities and velocity dispersions. The best-fitting templates (as numbered in Table 2) are given in the "Templates" column. The σ and v_{helio} values are the mean values using all observations of the best fitting template(s). In the cross-correlation method, σ and v_{helio} are the mean values using all stellar templates.

TABLE 5
ADOPTED RADIAL VELOCITY AND VELOCITY DISPERSION OF VIRGO CLUSTER OBJECTS

Object	$v_{\rm helio}$ (kms^{-1})	σ (kms^{-1})
Strom 417	1860.3 ± 1.5	27.6 ± 1.9
VUCD 1	1223.7 ± 1.5	34.1 ± 1.7
VUCD 3/Strom 547	713.5 ± 2.4	42.1 ± 1.5
VUCD 4	916.1 ± 1.6	23.9 ± 2.0
VUCD 5	1289.5 ± 1.4	28.2 ± 1.6
VUCD 6	2101.0 ± 1.6	25.2 ± 1.8
VUCD 7	984.5 ± 3.1	38.0 ± 4.1
VCC 1407	1018.9 ± 3.3	30.4 ± 2.6
NGC 4486B	1557.4 ± 6.5	205.2 ± 4.9

population contributions to the continuum is varying rapidly in this object compared to the other UCDs. This might be expected because this object also has a much higher metallicity than the other UCDs (see § 6), so that the relative contribution of the higher gravity dwarf stars to the blue-green (Mg *b*) region of the spectrum is greater, leading to broader lines in this region compared to the other UCDs. The CaT region is dominated by giant stars, no matter the metallicity of the UCDs. Modeling of this effect could lead to a better understanding of the stellar populations, but a more extensive library of stars is required.

3. IMAGING

We obtained images of the Virgo UCDs in the course of *HST* snapshot program 10137. The data were taken with the Advanced Camera for Surveys (ACS), High Resolution Channel (HRC), through the F606W and F814W filters. Exposure times were 870 s in F606W and 1050 s in F814W. The HRC scale is 0.025″ pixel^{-1}. For the image analysis we used MultiDrizzle[3] (*.mdz) files retrieved from the *HST* archive.

To measure the total magnitudes, we plotted curves of growth (integrated magnitude vs. circular aperture radius) to find an aperture radius large enough to enclose all the light from an object. The instrumental F606W and F814W magnitudes were transformed into Landolt *V* and *I* band following Sirianni et al. (2005). The resulting *V* magnitudes and $V - I$ colors are listed in Table 6.

We have also used *HST* imaging data (program 8685) for Fornax UCDs and a dE,N (FCC 303), initially presented in Drinkwater et al. (2003), as one of the aims of this work is to compare Virgo UCDs with Fornax UCDs and dwarf nuclei. The data consist of 1960 s exposures taken with the Space Telescope Imaging Spectrograph (STIS) in unfiltered mode (50CCD). The STIS has a scale of 0.0507″ pixel^{-1}. We reprocessed the STIS images with MultiDrizzle to ensure that the data reduction method for the Fornax UCD images was consistent with that of the Virgo UCD images. The instrumental AB magnitudes were transformed into *V* band using the relation

$$50\mathrm{CCD} = V + 0.2165 + 0.5831(B - V) - 2.267(B - V)^2 + 2.6626(B - V)^3 - 1.128(B - V)^4$$

(H. Ferguson 2000, private communication; see also Gregg & Minniti 1997). We used $B - V$ colors for UCDs and FCC 303 from Karick et al. (2003). The total *V* magnitudes for Fornax UCDs and FCC 303 are presented in Table 7.

[3] See http://stsdas.stsci.edu/multidrizzle/.

TABLE 6
VIRGO UCD PHOTOMETRY

Name	m_V (mag)	M_V (mag)	$V - I$ (mag)
VUCD 1	18.66	−12.26	0.96
VUCD 3/Strom 547	18.34	−12.58	1.27
VUCD 4	18.62	−12.30	0.99
VUCD 5	18.60	−12.32	1.11
VUCD 6	18.82	−12.10	1.02
VUCD 7	17.48	−13.44	1.13

NOTES.—The *V*-band apparent magnitude m_V is determined as described in § 3 and is corrected for foreground dust extinction (Schlegel et al. 1998). The absolute magnitude M_V is computed assuming a Virgo Cluster distance modulus of 30.92 mag (Freedman et al. 2001). The $V - I$ color is reddening-corrected.

TABLE 7
FORNAX UCDs AND A FORNAX dE,N (FCC 303): PHOTOMETRY

Object	R.A. (J2000.0)	Decl. (J2000.0)	m_V (mag)	M_V (mag)
UCD 1	03 37 03.30	−35 38 04.6	19.20	−12.19
UCD 2	03 38 06.33	−35 28 58.8	19.12	−12.27
UCD 3	03 38 54.10	−35 33 33.6	17.82	−13.57
UCD 4	03 39 35.95	−35 28 24.5	18.94	−12.45
UCD 5	03 39 52.58	−35 04 24.1	19.40	−11.99
FCC 303	03 45 14.08	−36 56 12.4	15.90	−15.49

NOTES.—The *V*-band apparent magnitude m_V is determined as described in § 3 and is corrected for foreground dust extinction (Schlegel et al. 1998). The absolute magnitude M_V is computed assuming a Fornax Cluster distance modulus of 31.39 mag (Freedman et al. 2001). Units of right ascension are hours, minutes, and seconds, and units of declination are degrees, arcminutes, and arcseconds.

The images of Virgo and Fornax UCDs were modeled using the two-dimensional fitting algorithm GALFIT (Peng et al. 2002) and assuming empirical King, Sérsic, and Nuker models for the luminosity profile.

The King profile is characterized by the core radius R_c and the tidal radius R_t and has the following form:

$$I(R) = I_0 \left\{ \frac{1}{\left[1 + (R/R_c)^2\right]^{1/\alpha}} - \frac{1}{\left[1 + (R_t/R_c)^2\right]^{1/\alpha}} \right\}^{\alpha}, \quad (1)$$

where I_0 is the central surface brightness. We tried both the standard model with $\alpha = 2$ and a generalized model with variable α. The King model provides a good fit to GC luminosity profiles when the concentration index $c = \log(R_t/R_c) = 0.75$–1.75 and to elliptical galaxy luminosity profiles if $c \geq 2.2$ (Mihalas & Binney 1981).

The Sérsic power law is often used to fit luminosity profiles of galaxies and has the following form:

$$I(R) = I_{\rm eff} \exp\left\{ -k \left[\left(\frac{R}{R_{\rm eff}} \right)^{1/n} - 1 \right] \right\}, \quad (2)$$

where $R_{\rm eff}$ is the half-light (effective) radius, $I_{\rm eff}$ is surface brightness at the effective radius, n is the concentration parameter ($n = 4$ for a de Vaucouleurs profile, and $n = 1$ for an exponential profile), and k is a constant that depends on n.

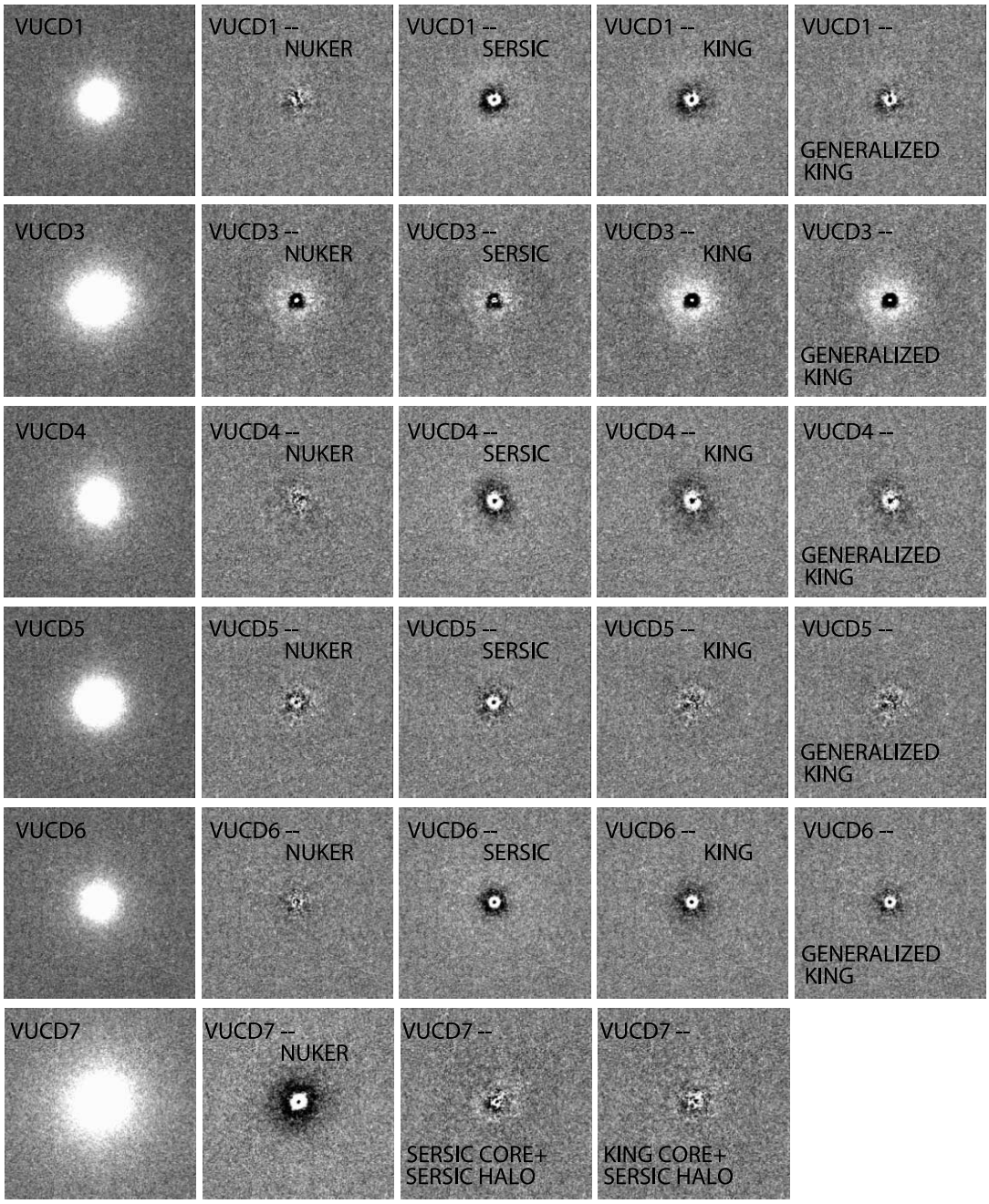

FIG. 1.— Virgo UCD images in the F606W filter (*first column*) and residual maps after subtracting (PSF-convolved) GALFIT models from the UCD images. All the images have a size of $\approx 5.4'' \times 5.4''$ ($\approx$401 pc $\times$ 401 pc).

The Nuker law is as follows:

$$I(R) = I_b 2^{(\beta-\gamma)/\alpha} \left(\frac{R}{R_b}\right)^{-\gamma} \left[1+\left(\frac{R}{R_b}\right)^{\alpha}\right]^{(\gamma-\beta)/\alpha}. \quad (3)$$

It is a double power law, where β is the outer power-law slope, γ is the inner slope, and α controls the sharpness of the transition (at the "break" radius R_b) from the inner to the outer region. Note that $I_b = I(R_b)$. The Nuker law was introduced by Lauer et al. (1995) to fit galaxy centers.

GALFIT convolves the analytic profile with the point-spread function (PSF) and determines the best-fitting model parameters by minimizing residuals between the model and original *two-dimensional* image.

We derived artificial PSFs for ACS HRC images in the F606W and F814W filters using the TinyTim software[4] and MultiDrizzle as follows. First, we generated ACS HRC PSFs with TinyTim; these include all the distortions, so they represent the PSF in raw images. We then implanted these PSFs in empty distorted images (*.flt files), *at the location of each target observed*, and passed them through MultiDrizzle using the same parameters as were used for the data. This produces model PSFs that are processed the same way as the real data. For the STIS imaging, the generation of the PSF is more straightforward and is achieved through a single pass of TinyTim.

The quality of the GALFIT model fits in the inner regions of each object is shown in Figures 1 and 2. These figures present

[4] See http://www.stsci.edu/software/tinytim/.

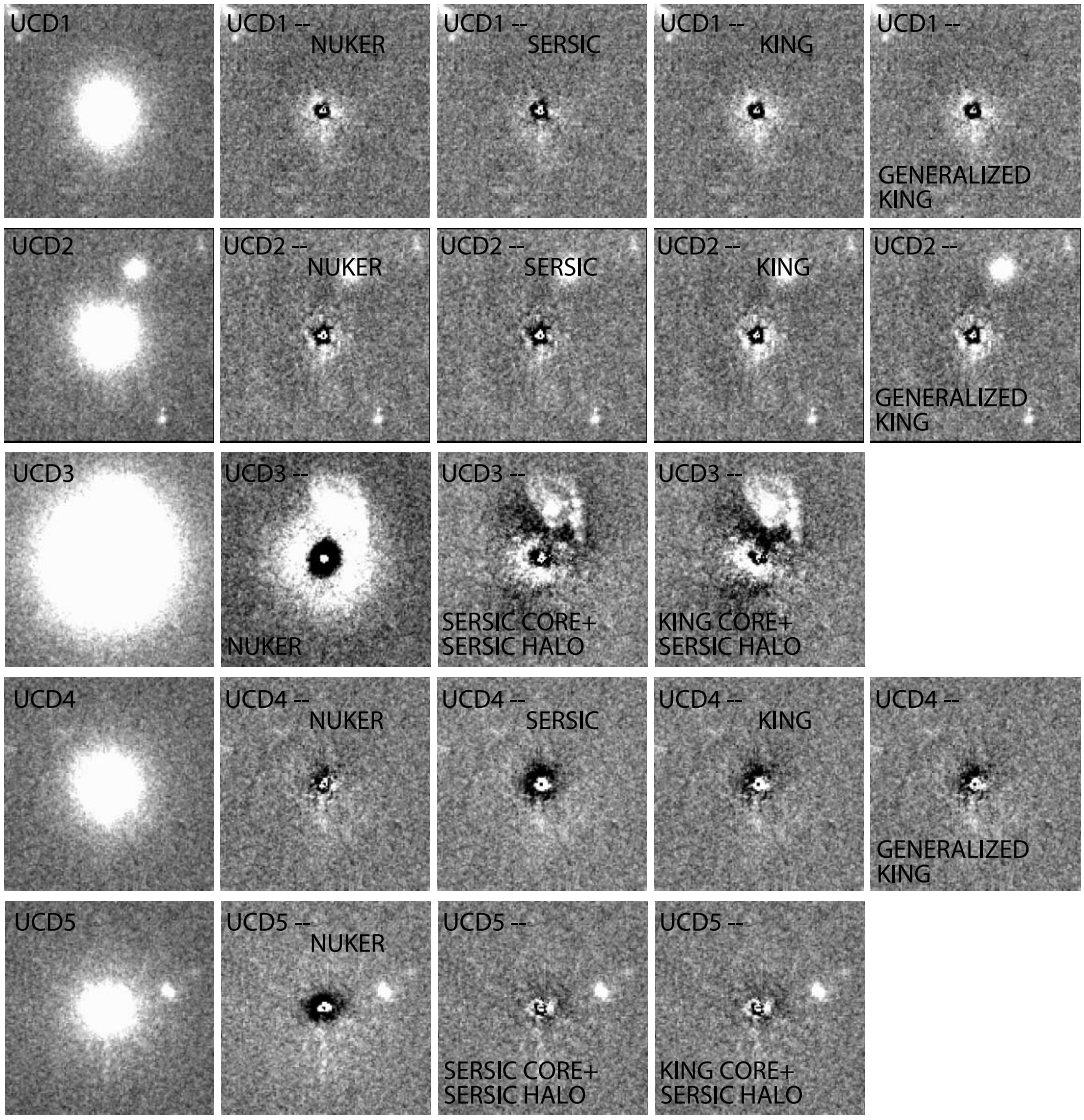

FIG. 2.—Fornax UCD images (*first column*) and residual maps after subtracting (PSF convolved) GALFIT models from the UCD images. All the images have a size of $\approx 6.6'' \times 6.6''$ (≈ 607 pc $\times$ 607 pc).

residual maps after subtracting the (PSF-convolved) model from each object. The quality of the models in the outer regions is better shown in Figures 3 and 4. For these figures we used the ELLIPSE task in IRAF to produce *one-dimensional* surface brightness profiles for the objects and (PSF-convolved) GALFIT models.

The χ^2_ν values of the fits (see Peng et al. 2002) are shown in Tables 8 and 9. We use χ^2_ν values to choose the *best model* for each object (see the last rows of Tables 8 and 9).

From Figures 1–4 and the χ^2_ν values *in both filters* we can see that the Virgo UCDs are poorly fitted with the standard King model ($\alpha = 2$), but are very well fitted with the Nuker law—a double power law (except VUCD 7, which requires a two-component model). King models predict a truncation radius, beyond which stars are stripped from the cluster by the galactic tidal field. *None of the UCDs show this tidal cutoff down to our limiting surface brightness*. Also, a main feature of King models is their central cores—the regions of constant surface brightness. We have found from Nuker models that only one UCD has a flat core (VUCD 5); all other UCDs have shallow or steep cusps in the center (Table 8).

Generalized King models (with a variable α-parameter) provide better fits to the data than standard King models. The parameter α controls both the slope of the profile and the transition from the main body into R_t. When we relax the α-parameter, we can better fit the extended outer parts of the UCDs. However, King models have a tidal cutoff and do not fit the data as well as untruncated Nuker models do.

To fit a standard King model to the F606W data for VUCD 3, we had to fix R_c at 1 pixel (1.9 pc). There is no convergency if we leave R_c as a free parameter (perhaps because R_c becomes too small, $\ll$1 pixel). The lack of a good King fit to the F606W data for VUCD 3 is seen in Figure 3. We also failed to fit any of the King models to the F814W data for this object. There was no convergency with R_c either fixed or relaxed.

Sérsic models do not provide good fits to the Virgo UCDs either. In the majority of cases, the model profiles drop faster than the data. The fit seems good in the case of VUCD 3, but this object has a very steep profile (a very high index n). Models with a Sérsic index $n > 2$ become very sensitive to the sky determination, flat-fielding, the accuracy of the PSF being used, and how well the assumed profile agrees with the data (see the online

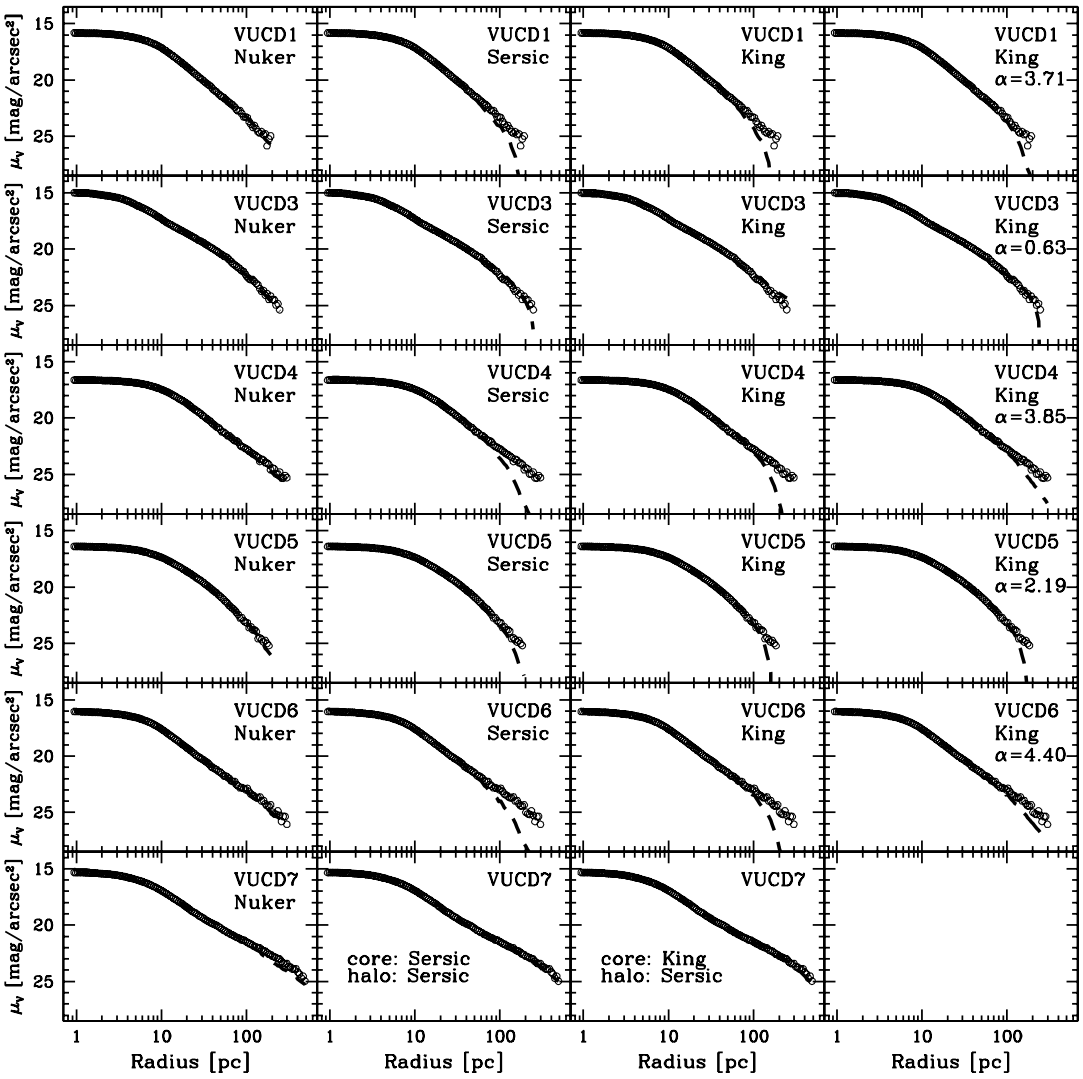

FIG. 3.—Surface brightness profiles for Virgo UCDs, measured in the F606W images. The instrumental magnitudes have been transformed into the V band. The open circles represent UCD profiles; the dashed line represents the best-fitting model convolved with the PSF.

GALFIT manual).[5] The more centrally concentrated a galaxy profile is (the larger the Sérsic index n is), the more extended an outer wing it has. Because of this behavior, if (for example) a profile already has a high intrinsic index n, a small underestimation of the background can make n even higher and can cause large errors in the magnitude and size. When fitting VUCD 3 data in the two passbands, we obtained quite different parameters: e.g., the difference in R_e was 39%. This could be due to the above reasons.

We conclude that the Nuker law appears to be the best model for all Virgo UCDs except VUCD 7, in which case the King core + Sérsic halo model is the best one.

The situation is different for the Fornax UCDs. There is no universal model for them. Two objects (UCD 3 and UCD 5) are best fitted by two-component models. The other three have very steep profiles that are hard to model. In the case of UCD 1 the best model is Sérsic. The best model for UCD 2 is the generalized King law, and in the case of UCD 4 it is the Nuker law.

The residual maps of Fornax UCD 3 reveal faint structure to the northwest of the core. This is very likely a background spiral galaxy along the line of sight. This structure affected the profile fits to UCD 3 to the extent that the two-component models gave very inconsistent results. For this object we therefore restricted the model fits to the bottom half of the image. The model parameters for UCD 3 in all the tables are from these fits to half the images, although we show the images and plots in Figures 2 and 4 for the whole-image fits to reveal the background object.

The UCD structural parameters obtained from the fits are summarized in Tables 8 and 9. The Nuker fits gave us the outer power-law slope β, the inner slope γ, the α-parameter, the break radius R_b, the surface brightness of the profile at the break radius $\mu_V(R_b)$, and ellipticity $\epsilon = 1 - b/a$ (b/a is the minor-to-major axial ratio). From Sérsic models, we obtained the half-light radius $R_{\rm eff}$, Sérsic index n, ellipticity ϵ, and the integrated magnitude $m_{V,\rm tot}$. The King fits gave us the core radius R_c, tidal radius R_t, concentration parameter $c = \log(R_t/R_c)$, central surface brightness $\mu_{0,V}$, and ellipticity ϵ. All the GALFIT models assume a constant ellipticity that is fitted at the same time as the other parameters. The $R_{\rm eff}$ values and the integrated magnitudes for the King and Nuker models were obtained via numerical integration of the luminosity profiles (defined by eqs. [1] and [3]). We also obtained half-light radii from the observational data directly ($R_{e,\rm obs}$).

[5] See http://zwicky.as.arizona.edu/~cyp/work/galfit/TFAQ.html.

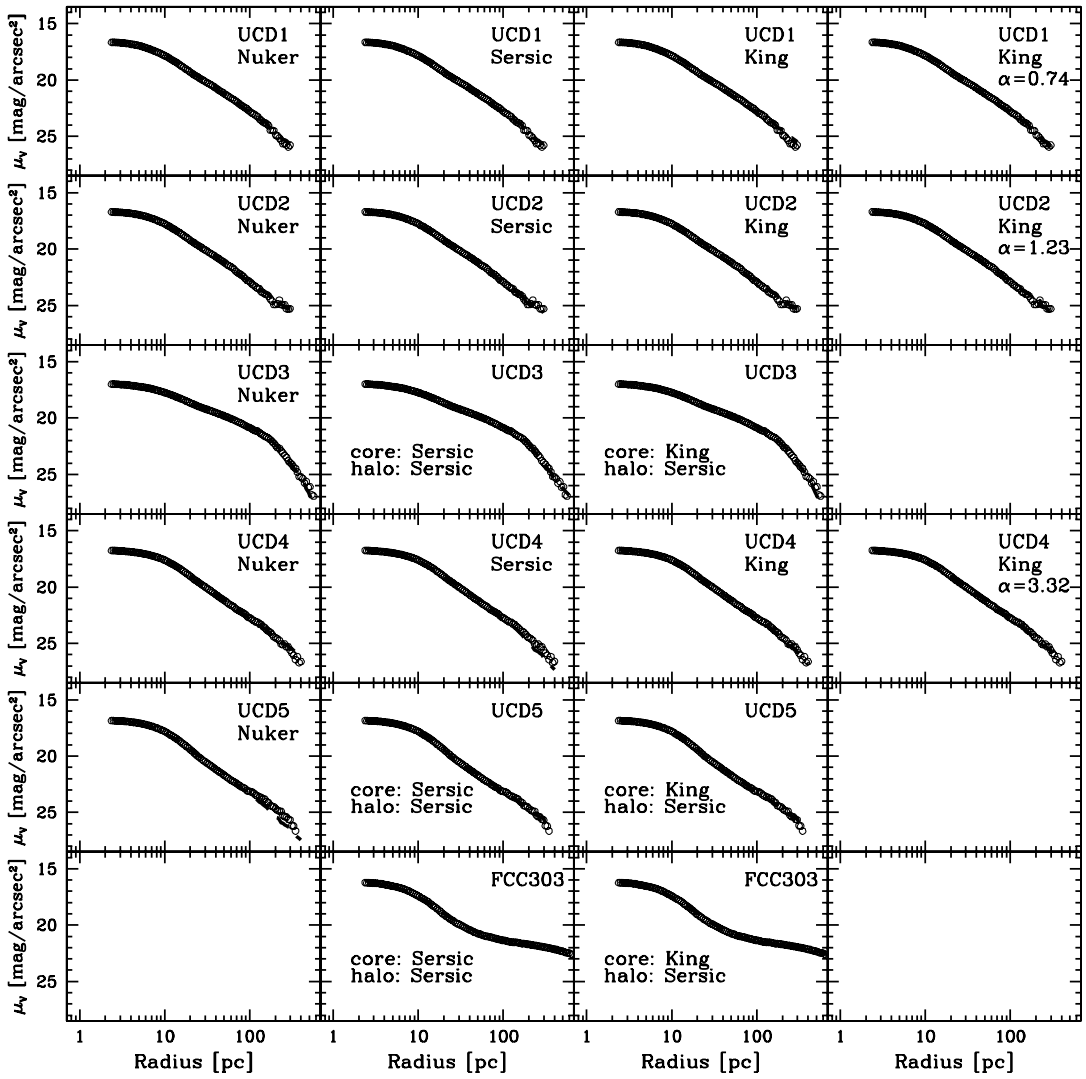

FIG. 4.—Surface brightness profiles for Fornax UCDs and a Fornax dE,N (FCC 303). The instrumental magnitudes have been transformed into the V band. The open circles represent UCD profiles; the dashed line represents the best-fitting model convolved with the PSF.

In this case, the data were not PSF-deconvolved, and the half-light radii may be overestimated. The structural parameters for Virgo UCDs were averaged between the two filters.

For further analysis we had to decide what $R_{\rm eff}$ to choose for our objects. We could not take just the best model $R_{\rm eff}$ because, for example, in the case of Virgo UCDs the best model is Nuker. For all the Nuker models in Tables 8 and 9 (except for VUCD 1 and VUCD 5) the total volume under the profile (the integrated luminosity) converges very slowly. It makes $R_{\rm eff}$ estimations uncertain and results in unphysically large $R_{\rm eff}$ values. This is why we chose generalized King $R_{\rm eff}$ values. The generalized King models fit the Virgo UCD data better than standard King and Sérsic models, and they are finite in extent. In addition to this, generalized King $R_{\rm eff}$ values are consistent with the observational half-light radii ($R_{e,\rm obs}$).

In the case of the Fornax UCDs we also chose the generalized King $R_{\rm eff}$ for one-component UCDs and the King $R_{\rm eff}$ for the cores of the two-component objects. The Sérsic fits seem unreliable, as all of the models have very high index n (see above). Nuker models are not good for $R_{\rm eff}$ estimation for the reason explained above.

We list the best values of the various parameters of the Virgo and Fornax objects in Table 10. These are used in § 4 for analysis of the scaling relations. In Table 10 we quote three values of effective radius $R_{\rm eff}$ in the case of two-component objects (VUCD 7, UCD 3, UCD 5, and FCC 303): the total, only the core, and only the halo. These were obtained via numerical integration of the model luminosity profiles. Table 10 also contains the total V-band apparent magnitude m_V, the mean surface brightness within the effective radius $\langle\mu_V\rangle_{\rm eff}$, and ellipticity ϵ. The m_V values are observational values copied from Tables 6 and 7, except for the core and halo magnitudes of the two-component objects, which are model values taken from Tables 8 and 9 (King + Sérsic models). The $\langle\mu_V\rangle_{\rm eff}$ values were derived from $R_{\rm eff}$ and m_V as follows:

$$\langle\mu_V\rangle_{\rm eff} = m_V + 5\log R_{\rm eff} + 1.995, \quad (4)$$

where $R_{\rm eff}$ is measured in arcseconds. The ϵ figures are the best model values from Tables 8 and 9.

The ellipticities of the UCDs given in Table 10 show that some of the objects are significantly noncircular; the maximum (core) ellipticity is 0.24 for Fornax UCD 5.

We have compared the distribution of UCD ellipticities with those reported for GCs in NGC 5128 (Harris et al. 2002) and the

TABLE 8
STRUCTURAL PARAMETERS FOR VIRGO UCDS FROM ACS HRC PHOTOMETRY

Parameter	VUCD 1	VUCD 3	VUCD 4	VUCD 5	VUCD 6	VUCD 7 Core	VUCD 7 Halo[a]
$R_{e,\mathrm{obs}}$	15.4	28.1	29.4	22.5	22.1	...	...
Nuker							
χ^2_ν (F606W)	0.39	0.41	0.35	0.38	0.24	...	...
χ^2_ν (F814W)	0.38	0.43	0.34	0.36	0.27	...	...
R_e	13.3	...	...	19.2	...	...	...
$m_{V,\mathrm{tot}}$	18.49	...	...	18.55	...	...	...
R_b	6.3	73.3	9.1	19.3	5.2	...	...
$\mu_V(R_b)$	16.42	22.00	17.24	18.73	16.45	...	...
α	2.52	1.95	3.92	0.99	19.48	...	...
β	2.69	3.17	2.34	4.02	2.24	...	...
γ	0.23	1.53	0.33	0.00	0.50	...	...
ϵ	0.06	0.15	0.15	0.01	0.04	...	...
Sérsic							
χ^2_ν (F606W)	0.48	0.42	0.40	0.39	0.29	0.37	0.37/0.37
χ^2_ν (F814W)	0.44	0.45	0.38	0.38	0.31	0.37	0.36/0.37
R_e	11.1	64.3	19.3	18.1	12.9	9.2	214.1/223.4
$m_{V,\mathrm{tot}}$	18.75	17.69	18.85	18.64	19.05	18.68	18.01/17.85
n	2.2	10.9	2.1	1.9	3.1	2.2	1.4/2.1
ϵ	0.07	0.16	0.16	0.01	0.04	0.12	0.05/0.05
King, $\alpha = 2$							
χ^2_ν (F606W)	0.45	0.55	0.37	0.37	0.27	0.37	...
χ^2_ν (F814W)	0.42	...	0.36	0.37	0.29	0.36	...
R_e	11.2	...	21.8	17.8	15.2	10.4	...
$m_{V,\mathrm{tot}}$	18.66	...	18.54	18.59	18.93	18.42	...
R_c	3.6	1.9	5.8	6.6	2.7	3.1	...
R_t	124.0	∞	302.7	172.5	355.6	130.2	...
c	1.54	...	1.71	1.42	2.12	1.62	...
$\mu_{0,V}$	14.91	13.79	15.96	15.98	14.98	14.38	...
ϵ	0.06	0.17	0.15	0.01	0.04	0.11	...
King with Variable α							
χ^2_ν (F606W)	0.41	0.53	0.36	0.37	0.25	...	...
χ^2_ν (F814W)	0.40	...	0.35	0.37	0.28	...	...
α	3.74	0.63	3.95	2.24	4.45	...	...
R_e	11.3	18.7	22.0	17.9	14.8	...	...
$m_{V,\mathrm{tot}}$	18.63	18.18	18.52	18.60	18.84	...	...
R_c	4.3	1.8	6.7	6.7	3.2	...	...
R_t	360.0	247.5	1217.4	200.5	2352.5	...	...
c	1.92	2.14	2.26	1.48	2.87	...	...
$\mu_{0,V}$	14.68	13.78	15.76	15.97	14.81	...	...
ϵ	0.06	0.17	0.15	0.01	0.04	...	...
Best model	N	N	N	N	N	K	S

NOTES.—All parameters are the mean of the two passbands, V and I, except the King models for VUCD 3 (see explanation in the text). Units: $R_{e,\mathrm{obs}}$, R_e, R_b, R_c, and R_t are in parsecs; $\mu_V(R_b)$ and $\mu_{0,V}$ are in mag arcsec^{-2}; and $m_{V,\mathrm{tot}}$ is in magnitudes. The $\mu_V(R_b)$, $\mu_{0,V}$, and $m_{V,\mathrm{tot}}$ values are corrected for extinction in our Galaxy.

[a] The first number is for a King + Sérsic model, and the second number is for a Sérsic + Sérsic model.

Milky Way (MW; Harris 1996; online catalog version of 2003 February). The two-sample Kolmogorov-Smirnov (K-S) test indicates that the UCD ellipticities are consistent with both the MW GC distribution (the significance level[6] is 53% or 66% depending on the ellipticity used for two-component UCDs, core or halo) and the NGC 5128 GC distribution (the significance level is 38% or 63%). The Wilcoxon test gives similar results: the UCD ellipticities are consistent with the MW GC distribution at the 42% or 36% significance level and with the NGC 5128 GC distribution at the 27% or 46% significance level.

4. FUNDAMENTAL PLANE RELATIONS

In this section we compare UCDs with GCs and galaxies by their position in both the luminosity–velocity dispersion plane and κ-space (the fundamental plane as defined by Bender et al. 1992).

First we revise the luminosity-velocity dispersion correlation for UCDs and other types of stellar systems proposed in

[6] By significance level we mean the (percentage) probability that the K-S test statistic is as large as measured for the null hypothesis that the data sets are drawn from the same distribution. Small values of the significance indicate that the distributions differ significantly.

TABLE 9

STRUCTURAL PARAMETERS FOR FORNAX UCDs AND A dE,N (FCC 303) FROM STIS PHOTOMETRY

Parameter	UCD 1	UCD 2	UCD 3	UCD 3 Core	UCD 3 Halo[a]	UCD 4	UCD 5 Core	UCD 5 Halo[a]	FCC 303 Core	FCC 303 Halo[a]
$R_{e,\rm obs}$	33.2	29.5	80.7	...	...	31.3	...	...	...	...
Nuker										
χ^2_ν	0.61	0.64	0.51	...	...	0.50	...	...	...	...
R_e	...	...	...	...	...	...	...	...	...	...
$m_{V,\rm tot}$	...	...	...	...	...	...	...	...	...	...
R_b	36.7	4.3	318.7	...	...	7.3	...	...	...	...
$\mu_V(R_b)$	20.67	16.53	24.38	...	...	16.92	...	...	...	...
α	0.34	0.73	1.90	...	...	20.00	...	...	...	...
β	3.03	2.38	7.04	...	...	2.13	...	...	...	...
γ	0.91	0.58	1.10	...	...	0.88	...	...	...	...
ϵ	0.18	0.01	0.03	...	...	0.05	...	...	...	...
Sérsic										
χ^2_ν	0.60	0.66	...	0.47	0.47/0.47	0.69	0.47	0.47/0.47	1.03	1.03/1.03
R_e	36.9	26.6	...	8.6	106.6/103.2	24.1	6.0	134.5/135.5	25.2	696.3/692.8
$m_{V,\rm tot}$	19.01	19.03	...	20.29	17.98/17.94	18.97	20.45	19.54/19.58	18.76	15.95/15.95
n	9.9	6.8	...	1.7	1.3/1.5	5.5	1.1	6.9/6.3	10.7	0.6/0.6
ϵ	0.19	0.01	...	0.02	0.03/0.03	0.05	0.24	0.16/0.15	0.03	0.10/0.10
King, $\alpha = 2$										
χ^2_ν	0.67	0.63	...	0.47	...	0.52	0.47	...	1.03	...
R_e	48.9	28.3	...	10.9	...	26.0	6.0	...	25.9	...
$m_{V,\rm tot}$	18.71	18.98	...	20.00	...	18.88	20.19	...	18.78	...
R_c	1.8	2.3	...	3.6	...	2.8	4.0	...	1.2	...
R_t	5761.2	1457.5	...	119.2	...	987.6	30.7	...	2403.9	...
c	3.51	2.80	...	1.52	...	2.55	0.89	...	3.30	...
$\mu_{0,V}$	14.21	14.70	...	15.74	...	14.89	15.13	...	13.32	...
ϵ	0.18	0.01	...	0.03	...	0.05	0.24	...	0.03	...
King with Variable α										
χ^2_ν	0.64	0.62	...	...	...	0.51	...	...	...	...
α	0.74	1.23	...	...	...	3.32	...	...	...	...
R_e	22.4	23.1	...	...	...	29.5	...	...	...	...
$m_{V,\rm tot}$	19.00	19.10	...	...	...	18.82	...	...	...	...
R_c	1.8	2.2	...	...	...	3.0	...	...	...	...
R_t	378.0	487.1	...	...	...	4501.2	...	...	...	...
c	2.32	2.35	...	...	...	3.18	...	...	...	...
$\mu_{0,V}$	14.21	14.67	...	...	...	14.94	...	...	...	...
ϵ	0.18	0.01	...	...	...	0.05	...	...	...	...
Best model	S	Gen. K	K+S/S+S	K	S	N	K/S	S	K/S	S

NOTES.—Units: $R_{e,\rm obs}$, R_e, R_b, R_c, and R_t are in parsecs; $\mu_V(R_b)$ and $\mu_{0,V}$ are in mag arcsec^{-2}; and $m_{V,\rm tot}$ is in magnitudes. The $\mu_V(R_b)$, $\mu_{0,V}$, and $m_{V,\rm tot}$ values are corrected for extinction in our Galaxy.

[a] The first number is for a King + Sérsic model, and the second number is for a Sérsic + Sérsic model.

Drinkwater et al. (2003). Figure 5 represents the absolute V magnitude versus central velocity dispersion relation for Fornax and Virgo UCDs, GCs (including the most massive and luminous ones: G1 in M31, the Galactic GC ω Cen, and NGC 5128 massive GCs) and galaxies. The UCD data were obtained in the present work (Tables 10 and 12), except central velocity dispersions for Fornax UCDs, which were taken from Hilker et al. (2007). The velocity dispersion for Fornax UCD 1 was derived from CaT region using the cross-correlation method and only one stellar template (G6/G8 IIIw type).[7] The data for GCs are from the following: M31 GCs, Djorgovski et al. (1997 and references therein); G1, Djorgovski et al. (1997 and references therein), except for half-light radius (required for Fig. 6), which was taken from Barmby et al. (2002); MW GCs, ω Cen, and LMC and SMC GCs (most of which have old ages) from McLaughlin & van der Marel (2005; photometry is based on Wilson models); NGC 5128 GCs, Martini & Ho (2004); Strom 417, spectroscopy from this work (Table 12), photometry from Haşegan et al. (2005). We also plot "dwarf globular transition objects" from Haşegan et al. (2005). Data for galaxies were obtained from the following: giant ellipticals, Faber et al. (1989); NGC 4486B, spectroscopy from our data and Bender et al. (1992), photometry from Faber et al. (1989); the compact elliptical galaxy M32, Faber et al. (1989) and Bender et al. (1992); dE,Ns and dwarf nuclei, Geha et al. (2002, 2003); FCC 303, photometry from this work, spectroscopy from Hilker et al. (2007); VCC 1407, velocity dispersion from this work, magnitude from the NASA/IPAC Extragalactic

[7] The UCD 1 velocity dispersion was measured and used by Drinkwater et al. (2003).

TABLE 10
ADOPTED PHOTOMETRIC PARAMETERS FOR VIRGO AND FORNAX UCDS AND THE FCC 303 GALAXY

Object	$R_{\rm eff}$ (pc)	m_V (mag)	$\langle\mu_V\rangle_{\rm eff}$ (mag arcsec^{-2})	ϵ
		Virgo		
VUCD 1.....	11.3	18.66	16.58	0.06
VUCD 3.....	18.7	18.34	17.34	0.15
VUCD 4.....	22.0	18.62	17.98	0.15
VUCD 5.....	17.9	18.60	17.51	0.01
VUCD 6.....	14.8	18.82	17.32	0.04
VUCD 7.....	96.8	17.48	20.06	...
VUCD 7 core.....	10.4	18.42	16.15	0.11
VUCD 7 halo.....	214.1	18.01	22.31	0.05
		Fornax		
UCD 1.....	22.4	19.20	18.13	0.19
UCD 2.....	23.1	19.12	18.12	0.01
UCD 3.....	89.7	17.82	19.76	...
UCD 3 core.....	10.9	20.00	17.36	0.03
UCD 3 halo.....	106.6	17.98	20.30	0.03
UCD 4.....	29.5	18.94	18.47	0.05
UCD 5.....	31.2	19.40	19.05	...
UCD 5 core.....	6.0	20.19	16.25	0.24
UCD 5 halo.....	134.5	19.54	22.37	0.16
FCC 303.....	660.0	15.90	22.18	...
FCC 303 core	25.9	18.78	18.03	0.03
FCC 303 halo	696.3	15.95	22.35	0.10

Database. All the M_V magnitudes were dereddened, and all the velocity dispersions for GCs and UCDs were aperture-corrected to give the standard values (the central velocity dispersions) used in the literature for the comparison with Galactic GCs.

From Figure 5 we can see that there is no gap between bright GCs and UCDs and that the Virgo UCDs have velocity dispersions and luminosities similar to those of the Fornax UCDs.

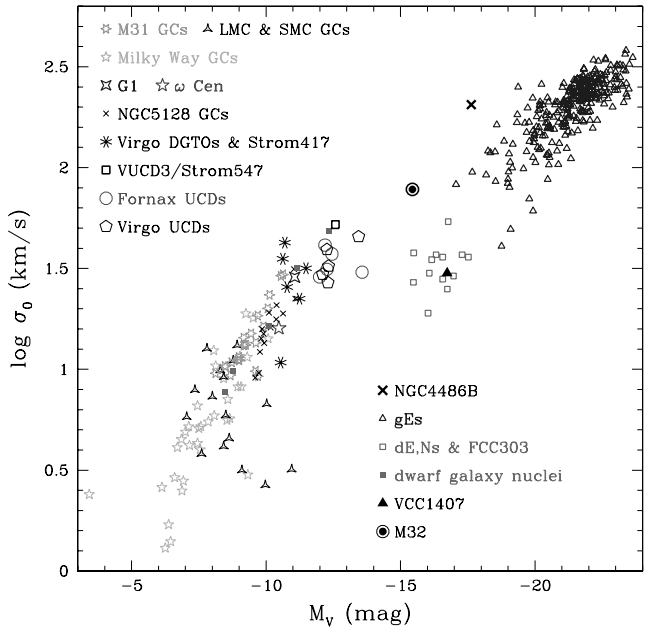

FIG. 5.—Comparison of the internal dynamics of UCDs with GCs and galaxies. The sources of the data are described in the text. [*See the electronic edition of the Journal for a color version of this figure*.]

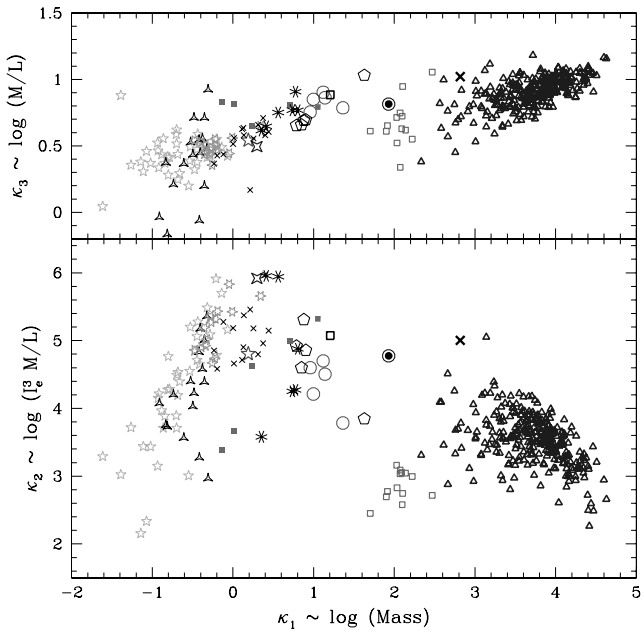

FIG. 6.—Fundamental plane for dynamically hot stellar systems (as defined by Bender et al. 1992). *Top*, Edge-on view; *bottom*, face-on view. Symbols are the same as in Fig. 7. The sources of the data are described in the text. [*See the electronic edition of the Journal for a color version of this figure*.]

VUCD 3/Strom 547 and Strom 417 were previously considered to be M87 GCs (Strom et al. 1981). These are the two brightest M87 GCs according to Hanes et al. (2001) list. Now we see that these GCs lie in the same part of M_V-σ_0 plane as UCDs and can be equally considered as UCDs. The UCDs, along with transition objects of Haşegan et al. (2005), appear to follow approximately the same relation between luminosity and velocity dispersion as old GCs. To make a firm conclusion as to whether the UCDs lie on the extrapolation of the GC relation, more data on the velocity dispersions for bright GCs (such as NGC 5128 and M31 GCs) or fainter UCDs (e.g., recently discovered in the Fornax Cluster; Drinkwater et al. 2004) are required. There is an overlap in the luminosities and velocity dispersions of the dE,N nuclei and the properties of bright GCs, transition objects of Haşegan et al., and UCDs, which is consistent with the stripping hypothesis for GC, transition object, and UCD formation.

Next we consider the location of UCDs relative to other stellar systems in the κ-space (Fig. 6). The κ-space is a space in which axes are combinations of three observable parameters (central velocity dispersion, effective radius, and mean intensity inside effective radius) into physically meaningful parameters. The κ-space parameters as defined by Bender et al. (1992) are as follows:

$$\kappa_1 \equiv \left(\log \sigma_0^2 + \log R_{\rm eff}\right)/\sqrt{2}, \tag{5}$$

$$\kappa_2 \equiv \left(\log \sigma_0^2 + 2\log I_{\rm eff} - \log R_{\rm eff}\right)/\sqrt{6}, \tag{6}$$

$$\kappa_3 \equiv \left(\log \sigma_0^2 - \log I_{\rm eff} - \log R_{\rm eff}\right)/\sqrt{3}, \tag{7}$$

where σ_0 is the central velocity dispersion in km s^{-1}, $R_{\rm eff}$ is the half-light radius in kiloparsecs, and $I_{\rm eff}$ is the mean intensity inside $R_{\rm eff}$, defined as $10^{-0.4(\langle\mu_V\rangle_{\rm eff}-26.42)}$ and measured in V-band solar luminosities pc^{-2}. The κ-variables have the following physical meanings: κ_1 is proportional to the logarithm of the mass, κ_2 is proportional to the logarithm of the surface brightness cubed

times the M/L ratio, and κ_3 is proportional to the logarithm of the M/L ratio.

As expected, objects are distributed more widely in the κ_1-κ_2 plane, the face-on projection of the fundamental plane, than in the κ_1-κ_3 plane, the edge-on projection. In the κ_1-κ_3 plane we show that the UCDs lie on the same tight correlation between mass and M/L ratio as the bright GCs and transition objects of Haşegan et al. (2005), but the fainter GCs ($\kappa_1 < 0$) show little if any correlation in this plane. This corresponds approximately to a mass of $10^6\ M_\odot$, at which Haşegan et al. (2005) also find a turnover in scaling relations for GCs and other low-mass systems in other projections of the fundamental plane. Consistent with previous discussions (e.g., Burstein et al. 1997), we find that this relation does not intersect that of giant elliptical galaxies in the same κ_1-κ_3 plane.

By contrast, in the κ_1-κ_2 plane we find that the UCDs are clearly not on the main GC relation (as defined by the MW and M31 GCs). The UCDs lie in a region away from this sequence in the direction of increasing mass (κ_1). The NGC 5128 GCs also lie off the main GC relation between it and the UCDs. We must note here that the UCDs are from magnitude-limited samples (equivalent to $0.6 < \kappa_1$), so these data do not actually provide evidence for a gap between UCDs and GCs. There is a relatively empty region in the plane at (κ_1, κ_2) values of around (0, 3.5–4.5) at masses intermediate between GCs and UCDs but low κ_2 values. According to Bastian et al. (2006), young massive star clusters, if evolved to ages of 10 Gyr, would occupy this region of the fundamental plane. Bastian et al. note that not many of these are expected to survive to such ages, but even those not disrupted would be unlikely to appear in the existing observational data sets due to the following selection effects. First, there are no UCDs in this region, as our UCD samples are limited to higher masses (luminosities, strictly speaking). Second, GCs in this region would have high mass and presumably would only be found in external galaxies like the NGC 5128 objects, but they would have much lower surface brightness values, so it would not be possible to measure their velocity dispersions even if they could be detected.

It is interesting to note that the more massive objects ($0 < \kappa_1 < 1.5$) show the opposite correlation between κ_1 and κ_2 to the lower mass systems in Figure 6. Since κ_3 (M/L) is increasing for the high-mass objects, it must be I_e^3 that is decreasing for these objects. This agrees with the mass-size relation observed for objects in this mass range (e.g., Kissler-Patig et al. 2006; Haşegan et al. 2005).

In both fundamental plane projections we also show the parameters of the nuclei of a sample of nucleated dwarf elliptical galaxies in the Virgo Cluster (Geha et al. 2002). The nuclei with masses similar to those of the UCDs lie in the same region of both plots as the UCDs. This is consistent with the threshing hypothesis for UCD formation from disrupted dwarf elliptical galaxies. The UCDs are mostly well separated from complete dwarf elliptical galaxies in the fundamental plane; the closest galaxy to UCDs is M32, the prototype "compact elliptical" galaxy that is also thought to have formed through a disruptive process (e.g., Choi et al. 2002).

5. MASSES AND MASS-TO-LIGHT RATIOS

In this section we estimate the masses of the UCDs using dynamical models. The masses and M/L ratios of the UCDs are important physical parameters for the understanding of their origin. In particular, the M/L ratio is an indicator for possibly existing dark matter and/or violation of dynamical equilibrium or isotropy of stellar orbits. If UCDs were the counterparts of GCs, one would expect M/L values as predicted by simple stellar population (SSP) models (e.g., Bruzual & Charlot 2003; Maraston 2005). If UCDs were of "galaxian origin"—formed in dark matter halos—they might still be dominated by dark matter and show high M/L values. M/L ratios larger than expected from SSPs can, however, also be caused by objects that are out of dynamical equilibrium, e.g., tidally disturbed stellar systems (Fellhauer & Kroupa 2006).

5.1. *Method*

The UCD masses were estimated from the measured velocity dispersions and their structural parameters. We showed in § 3 that the UCD light profiles can be fitted by various functions. A simple King profile often is not the best choice to represent UCD surface brightness profiles. However, most mass estimators available in the literature are based on the assumption of a King profile. In order to be not restricted to King profiles, we used a more general approach, using software developed by H. Baumgardt (see Hilker et al. 2007).

The first stage is to deproject the observed density profile (either King, generalized King, Sérsic, Nuker, or King + Sérsic), calculate its distribution function $f(E)$ under the assumption of spherical symmetry and an underlying isotropic velocity distribution, and finally create an N-body representation of the UCD. It is assumed that mass follows light (e.g., mass segregation is neglected). Besides the projected profile parameters, the total mass of the stellar system and the number of test particles are needed. The resulting model is a list of x, y, and z positions and v_x, v_y, and v_z velocities for all particles that correspond to the specified structural parameters and the given mass. From this model, the central as well as the global projected velocity dispersion can be calculated. The projected half-mass radii for all the models were also derived and were in very good agreement with the half-light radius values in Tables 8 and 9.

In the second stage, the velocity dispersion seen by an observer is simulated. In order to do this, all test particles are convolved with a Gaussian whose FWHM corresponds to the observed seeing. The fraction of the light (Gaussian) falling into the slit at the projected distance of the observed object (the size of the slit in arcseconds and the distance to the object in megaparsecs are input parameters) is then calculated. These fractions are used as weighting factors for the velocities. The weighted velocities of all particles whose "light" falls into the slit region are then used to calculate the mimicked observed velocity dispersion $\sigma_{\rm mod}$.

The total "true" mass of the modeled object, $M_{\rm true}$, which corresponds to the observed velocity dispersion $\sigma_{\rm obs}$, is not known a priori. One has to start with a first guess of the total mass, $M_{\rm guess}$, from which the "true" mass can be calculated as $M_{\rm true} = M_{\rm guess}(\sigma_{\rm obs}/\sigma_{\rm mod})^2$.

In the case of the Nuker and Sérsic functions, the models were truncated at large radii to avoid the unphysical infinite extensions of UCD light profiles. The truncation radius of the Nuker model was fixed to 2 kpc. The truncation radius of the Sérsic model was set to 20 times the effective radius, thus ranging between a few hundred parsecs and a few kiloparsecs for the UCDs in our sample. The true tidal radii of the UCDs depend on their distances to the cluster center R_G and the enclosed mass m_c of the potential they are living in. They can be estimated by the formula: $r_t = (Gm_c/2v_{\rm circ}^2)^{1/3}R_G^{2/3}$, where $v_{\rm circ}$ is the circular velocity of the cluster potential and G is the gravitational constant. The estimated tidal radii of the UCDs range between 1 and 4 kpc, thus justifying the chosen truncation radii.

A more detailed description of the mass determination process and mass values for Fornax UCDs are presented in Hilker et al. (2007). In this paper the discussion is focused on the Virgo UCDs.

TABLE 11

Dynamical Modeling Results for Different Light Profile Representations

Object	σ_0 (km s^{-1})	σ (km s^{-1})	M (10^7 $M_\odot$)	M/L_V ($M_\odot/L_\odot$)
Nuker				
VUCD 1	40.0 ± 1.2	30.7 ± 2.6	3.2 ± 0.5	4.5 ± 0.8
VUCD 3	$81.3 \pm 15.$	33.7 ± 10.4	1.8 ± 0.9	2.0 ± 1.0
VUCD 4	27.3 ± 1.5	19.7 ± 3.0	2.9 ± 0.7	4.0 ± 1.1
VUCD 5	31.5 ± 1.5	26.1 ± 2.5	3.0 ± 0.5	4.1 ± 0.8
VUCD 6	28.3 ± 1.0	20.6 ± 3.6	2.2 ± 0.6	3.7 ± 1.1
Sérsic				
VUCD 1	40.1 ± 1.6	32.7 ± 2.2	2.6 ± 0.3	3.8 ± 0.6
VUCD 3	61.0 ± 4.5	31.1 ± 9.0	5.7 ± 2.6	6.1 ± 2.8
VUCD 4	26.8 ± 1.4	22.3 ± 2.5	2.1 ± 0.5	3.0 ± 0.7
VUCD 5	31.5 ± 1.6	26.5 ± 1.9	2.9 ± 0.4	3.9 ± 0.6
VUCD 6	30.2 ± 0.8	23.4 ± 3.1	1.5 ± 0.4	2.5 ± 0.7
King, $\alpha = 2$				
VUCD 1	39.8 ± 0.8	32.6 ± 2.4	2.7 ± 0.4	3.9 ± 0.6
VUCD 4	27.7 ± 1.1	21.8 ± 2.8	2.4 ± 0.6	3.3 ± 0.8
VUCD 5	31.6 ± 0.7	26.4 ± 2.0	2.9 ± 0.4	3.9 ± 0.6
VUCD 6	30.5 ± 0.6	22.7 ± 5.3	1.8 ± 0.7	2.9 ± 1.3
Strom 417	31.7 ± 1.4	26.4 ± 2.7	2.7 ± 0.5	6.6 ± 1.5
King with Variable α				
VUCD 1	39.3 ± 2.0	32.2 ± 2.4	2.8 ± 0.5	4.0 ± 0.7
VUCD 3	52.2 ± 2.5	35.8 ± 1.5	5.0 ± 0.7	5.4 ± 0.9
VUCD 4	26.9 ± 2.3	21.3 ± 2.0	2.4 ± 0.6	3.4 ± 0.9
VUCD 5	32.5 ± 2.3	26.4 ± 1.6	2.9 ± 0.4	3.9 ± 0.6
VUCD 6	29.6 ± 2.2	22.3 ± 1.8	1.8 ± 0.5	2.9 ± 0.9
King Core + Sérsic Halo				
VUCD 7	45.1 ± 1.5	27.2 ± 4.6	8.8 ± 2.1	4.3 ± 1.1

Note.—Parameters: σ_0, central velocity dispersion; σ, global velocity dispersion; M, mass; M/L_V, M/L ratio.

5.2. *Uncertainty Analysis*

The uncertainties of the modeled masses were estimated from the uncertainty in the observed velocity dispersion $\Delta\sigma$ and the differences of the model parameters for surface brightness profiles in the V and I bands. On one hand, maximum and minimum model masses were simulated that correspond to the observed velocity dispersion of $(\sigma_{\rm obs} + \Delta\sigma)$ and $(\sigma_{\rm obs} - \Delta\sigma)$, respectively. The average of the differences $(M_{\rm max} - M_{\rm true})$ and $(M_{\rm true} - M_{\rm min})$ defines the first mass uncertainty. On the other hand, models were created that simulate $\sigma_{\rm obs}$ from the profile parameters in V and I separately, as well as from combinations of their parameters (i.e., R_c of V and R_t of I) to mimic the uncertainties in the profile parameters. The maximum and minimum mass deviations from $M_{\rm true}$ define the second uncertainty. Both uncertainties then were summed to derive the total mass uncertainty.

The uncertainties for the M/L ratios were propagated from the mass uncertainties and the uncertainty in the luminosity (assumed to be 0.05 mag in the absolute magnitude). The luminosities were derived from the apparent V magnitudes given in Table 10, the distance to the Virgo Cluster as mentioned in the introduction, and a solar absolute V magnitude of $M_{V,\odot} = 4.85$ mag.

The uncertainty of the central velocity dispersion was estimated from the observational uncertainty plus the scatter of modeled velocity dispersions in annuli of 0.5 pc within the central 5 pc for each object. The uncertainty of the global velocity dispersion is the sum of the observational uncertainty and the uncertainties as propagated from the mass uncertainty of the profile fitting parameters.

TABLE 12

Adopted Velocity Dispersions (Central and Global), Masses, and Mass-to-Light Ratios for Virgo UCDs

Object	σ_0 (km s^{-1})	σ (km s^{-1})	M (10^7 $M_\odot$)	M/L_V ($M_\odot/L_\odot$)
VUCD 1	39.3 ± 2.0	32.2 ± 2.4	2.8 ± 0.5	4.0 ± 0.7
VUCD 3	52.2 ± 2.5	35.8 ± 1.5	5.0 ± 0.7	5.4 ± 0.9
VUCD 4	26.9 ± 2.3	21.3 ± 2.0	2.4 ± 0.6	3.4 ± 0.9
VUCD 5	32.5 ± 2.3	26.4 ± 1.6	2.9 ± 0.4	3.9 ± 0.6
VUCD 6	29.6 ± 2.2	22.3 ± 1.8	1.8 ± 0.5	2.9 ± 0.9
VUCD 7	45.1 ± 1.5	27.2 ± 4.6	8.8 ± 2.1	4.3 ± 1.1
Strom 417	31.7 ± 1.4	26.4 ± 2.7	2.7 ± 0.5	6.6 ± 1.5

Note.—The values are based on the generalized King models for the one-component fits and on King + Sérsic models for the two-component fits.

5.3. *Results*

The results of the modeled object masses and velocity dispersions for the King, generalized King, Sérsic, Nuker, and King + Sérsic functions are presented in Table 11. These results are based on the surface brightness profile parameters in Table 8 and the observed velocity dispersions in Table 5. For Strom 417 we used surface brightness profile parameters obtained by Haşegan et al. (2005) from King model fits.

The masses and M/L values of the different models in general agree with each other within the uncertainties. On average, the masses of the Nuker profile models are slightly higher than those derived from the other profiles, whereas the masses of the Sérsic profile models are on the low side. As discussed in § 3, the generalized King models give the most stable estimates in the case of one-component profile fits. Therefore, the masses from the generalized King models and from the King core plus Sérsic halo models in the case of VUCD 7 were adopted for further analyses (see Table 12).

The Virgo UCDs have masses and M/L ratios in the range $M \approx (2\text{–}9) \times 10^7\ M_\odot$ and $M/L \approx (3\text{–}5)\ M_\odot/L_{\odot,V}$. The Fornax UCD masses and M/L ratios are in the same range (Hilker et al. 2007).

In order to compare our results with other dynamical mass estimators, we calculated masses using the King mass estimator (e.g., Queloz et al. 1995) and the virial mass estimator (Spitzer 1987). Both methods assume a constant M/L ratio as function of radius, an isotropic velocity distribution, and that the object is in virial equilibrium. We consider the UCDs to be in virial equilibrium, as their ages (estimated in § 6) are much greater than their crossing times ($T_{\rm cr} \sim R_{\rm eff}/\sigma \approx 0.4\text{–}4$ Myr).

The King mass estimator takes the form

$$M_{\rm K} = \frac{9}{2\pi G}\frac{\mu R_c \sigma_0^2}{\alpha p}, \tag{8}$$

where σ_0 is the central projected velocity dispersion (from Table 11, standard King model), R_c is the core radius (from Tables 8 and 9, standard King model), G is the gravitational constant, and μ, α, and p are constants that depend on the concentration c and are tabulated in King (1966) and Peterson & King (1975). The μ, α, and p values are the mean of the two passbands for Virgo UCDs, except for VUCD 6. In the case of VUCD 6 we used the V passband only, as

TABLE 13
Masses and Mass-to-Light Ratios from King and Virial Mass Estimators

Object	M_K ($10^7\ M_\odot$)	M_K/L_V ($M_\odot/L_\odot$)	M_{vir} ($10^7\ M_\odot$)	M_{vir}/L_V ($M_\odot/L_\odot$)
VUCD 1	2.9 ± 0.1	4.1 ± 0.3	2.7 ± 0.4	3.8 ± 0.7
VUCD 3	...	...	5.4 ± 0.7	5.8 ± 0.8
VUCD 4	2.5 ± 0.2	3.5 ± 0.3	2.3 ± 0.5	3.1 ± 0.7
VUCD 5	2.8 ± 0.1	3.7 ± 0.2	2.8 ± 0.4	3.8 ± 0.6
VUCD 6	2.1 ± 0.1	3.5 ± 0.3	1.7 ± 0.4	2.8 ± 0.8
VUCD 7	...	...	16.2 ± 5.7	7.9 ± 2.9
Strom 417	2.2 ± 0.2	5.6 ± 0.9	2.2 ± 0.5	5.4 ± 1.3

the I passband gives an unreasonably high mass estimate. The R_c, μ, α, and p values for Strom 417 were taken from Haşegan et al. (2005).

The virial mass estimator is as follows:

$$M_{vir} \approx 9.75 \frac{R_{eff}\sigma^2}{G}, \quad (9)$$

where σ is the global projected velocity dispersion (from Table 12) and R_{eff} is the half-light radius (from Table 10). The R_{eff} value for Strom 417 was taken from Haşegan et al. (2005).

The results of these two mass estimators are given in Table 13. The uncertainties of the calculated masses were propagated from the uncertainties in R_c and σ_0 for the King mass estimator and the uncertainties in R_{eff} and σ for the virial mass estimator, where the uncertainty in R_c was estimated from the difference of R_c in the V and I profile.

Both the King and the virial masses are consistent with the masses and M/L ratios indicated in Figure 6, and with the masses derived from the dynamical models (Table 12). The exception is VUCD 7 for which the virial mass estimate is 1.8 times larger than the dynamical model mass. This may be due to the inability of the simple virial estimator to correctly model the prominent core structure of this object, but the difference is not significant given the large uncertainty in the virial mass estimate for this object.

In Table 14 we compare the dynamical M/L estimates for Virgo UCDs with the predicted stellar M/L ratios of SSP models by Maraston (2005). To obtain the SSP model values, we used UCD ages and metallicities derived in § 6 (Fig. 9). The uncertainties of the M/L values are based on the age and metallicity ranges. The dynamical M/L values are consistent with the SSP model predictions within the uncertainties for both Salpeter and Kroupa initial mass functions (IMFs). It implies that Virgo UCDs do not require dark matter to explain their M/L ratios. This conclusion applies to the central region, where we have velocity dispersion data covered by our spectroscopic observations. An increasing dark matter contribution toward larger radii cannot be ruled out with the present data.

The M/L ratios of Fornax UCDs are discussed in Hilker et al. (2007).

The M/L ratio of Strom 417 (6.6 ± 1.5) is larger than the M/L value predicted by the SSP models with a Kroupa IMF, but is in agreement (within the uncertainties) with the predictions from the models with a Salpeter IMF. This M/L ratio is consistent with the high value reported for this object by Haşegan et al. (2005), but our result is based on their King model fit to this object. For this reason our measurement is not an independent confirmation of their result.

6. AGES AND CHEMICAL COMPOSITIONS

In this section we estimate the ages, metallicities, and abundances of our objects using the Lick/IDS index analysis. Lick/IDS absorption-line indices were measured as defined by Worthey et al. (1994) in the wavelength region 4800–6500 Å. We could not use the spectral region 3900–4800 Å due to low S/N. The line indices Hβ, Mg b, Fe λ5270, and Fe λ5335, together with 1 σ uncertainties, are listed in Table 15. Before measuring the indices we shifted the spectra to the rest-frame wavelengths. Since our spectra have much higher resolution ($\sigma_{ESI} \approx 0.3$ Å in the blue wavelength range) than the Lick/IDS system ($\sigma_{Lick} \approx 3.6$ Å at the Hβ–Fe λ5335 wavelength range), we smoothed our spectra to the resolution of the Lick data with a Gaussian of dispersion $(\sigma^2_{Lick} - \sigma^2_{ESI})^{1/2} \approx \sigma_{Lick}$. The estimated size of the smoothing kernel is $\sim$17 ESI pixels (Gaussian σ). After broadening, the Lick indices for our objects and for the Lick/IDS standards (nine stars) were measured as described in Worthey et al. (1994). The uncertainties on the indices were calculated according to Cardiel et al. (1998) based on the noise spectrum of each galaxy/GC.

To check the agreement between our instrumental system and Lick/IDS system, we calculated the difference between measured and published (Worthey et al. 1994) indices for all observations of the nine calibration stars. Figure 7 shows our standard-star measurements versus the published values (Worthey et al. 1994). The mean offsets between our instrumental system and the Lick/IDS system are listed in Table 16. The index measurements were corrected for the offsets.

The Lick index measurements for the NGC 4486B galaxy were also corrected for the effects of internal velocity dispersion as described in Davies et al. (1993). UCDs, GCs, and dE,Ns have small internal velocity dispersions compared to the Lick/IDS broadening function. There is no need to apply velocity dispersion correction for these objects.

We have not corrected the dE,N (VCC 1407) spectrum for any halo contribution because the nuclear light dominates in the

TABLE 14
Mass-to-Light Ratios and $V-I$ Colors for Virgo UCDs from SSP Models by Maraston (2005) in Comparison to the Dynamical Mass-to-Light Ratios and Observed $V-I$ Colors

Object	Age Range (Gyr)	Metallicity Range (dex)	$(V-I)_{obs}$ (mag)	$(V-I)_{sp}$ (mag)	$(V-I)_{kr}$ (mag)	$(M/L_V)_{dyn}$ ($M_\odot/L_\odot$)	$(M/L_V)_{sp}$ ($M_\odot/L_\odot$)	$(M/L_V)_{kr}$ ($M_\odot/L_\odot$)
VUCD 1	8–15	−1.35 to −0.33	0.96	0.91–1.16	0.89–1.13	4.0 ± 0.7	4.5 ± 1.9	2.9 ± 1.2
VUCD 3	12–15	0.00–0.35	1.27	1.19–1.30	1.16–1.27	5.4 ± 0.9	8.7 ± 2.1	5.6 ± 1.4
VUCD 4	8–15	−1.35 to −0.33	0.99	0.91–1.16	0.89–1.13	3.4 ± 0.9	4.5 ± 1.9	2.9 ± 1.2
VUCD 5	8–15	−0.33–0.00	1.11	1.07–1.22	1.05–1.20	3.9 ± 0.6	6.1 ± 2.3	3.9 ± 1.5
VUCD 6	8–15	−1.35 to −0.33	1.02	0.91–1.16	0.89–1.13	2.9 ± 0.9	4.5 ± 1.9	2.9 ± 1.2
VUCD 7	8–15	−1.35 to −0.33	1.13	0.91–1.16	0.89...1.13	4.3 ± 1.1	4.5 ± 1.9	2.9 ± 1.2
Strom 417	4–12	−1.35–0.00	...	0.82–1.19	0.81–1.16	6.6 ± 1.5	4.1 ± 2.6	2.6 ± 1.6

Note.—Here "sp" denotes results for a Salpeter IMF, and "kr" denotes results for a Kroupa IMF.

TABLE 15
LICK/IDS INDICES

Object	Hβ (Å)	Mg *b* (Å)	Fe λ5270 (Å)	Fe λ5335 (Å)	⟨Fe⟩ (Å)	[MgFe]′ (Å)
VUCD 1	2.06 ± 0.14	2.20 ± 0.13	1.56 ± 0.15	1.19 ± 0.17	1.38 ± 0.16	1.79 ± 0.15
VUCD 3/Strom 547	1.40 ± 0.14	4.99 ± 0.12	2.69 ± 0.13	2.37 ± 0.15	2.53 ± 0.14	3.60 ± 0.14
VUCD 4	2.16 ± 0.18	1.42 ± 0.16	1.41 ± 0.18	1.18 ± 0.21	1.30 ± 0.20	1.38 ± 0.17
VUCD 5	1.82 ± 0.17	3.30 ± 0.15	2.11 ± 0.17	1.90 ± 0.19	2.01 ± 0.18	2.60 ± 0.17
VUCD 6	2.27 ± 0.16	1.58 ± 0.15	1.40 ± 0.17	0.87 ± 0.19	1.14 ± 0.18	1.41 ± 0.17
VUCD 7	1.90 ± 0.32	2.45 ± 0.29	1.75 ± 0.33	1.09 ± 0.38	1.42 ± 0.36	1.96 ± 0.33
Strom 417	2.18 ± 0.23	2.86 ± 0.20	1.82 ± 0.23	1.47 ± 0.25	1.65 ± 0.24	2.22 ± 0.23
VCC 1407	2.08 ± 0.24	2.20 ± 0.21	1.63 ± 0.24	1.53 ± 0.27	1.58 ± 0.26	1.88 ± 0.24
NGC 4486B	1.39 ± 0.04	5.24 ± 0.04	2.93 ± 0.04	2.60 ± 0.05	2.77 ± 0.05	3.86 ± 0.04

central 1.5″ of our extraction; this object is already on the old envelope, and its indices agree well with the other Virgo dwarf elliptical galaxies measured by Geha et al. (2003).

The NGC 4486B galaxy does not have a distinct halo like the dEs do, and the problem is the opposite of the dE problem. When subtracting "sky" from along the short slit like ESI (20″), one really subtracts a component of galaxy light from farther out, so then one ends up subtracting too much stellar light, which then alters the actual physical extent of what one samples. However, since ellipticals (especially the likes of NGC 4486B) are very peaked in the center and have very modest (if any) line-strength gradients, the error in the measured indices is very small.

To translate measured line indices into age and metallicity estimates, we used the SSP models of Thomas et al. (2003). These models predict Lick indices for a wide range of ages (1—15 Gyr) and metallicities ($[Z/H] = -2.25$, -1.35, -0.33, 0.0, +0.35, and +0.67 dex), and are tabulated for several different abundance ratios ($[\alpha/Fe] = -0.3$, 0.0, +0.3, and +0.5).

To estimate $[\alpha/Fe]$ for the UCDs, we plot Mg *b* (an indicator of $\alpha-$elements) versus ⟨Fe⟩ (an average of the indices Fe λ5270 and Fe λ5335) in Figure 8, overlaid with isochrones and isometallicity lines from Thomas et al. (2003). Five UCDs and Strom 417 (a GC) have supersolar abundance ratio, $[\alpha/Fe] \approx +0.3-+0.5$, and one UCD appears to have solar abundances, $[\alpha/Fe] \approx 0.0$. The supersolar abundances ($[\alpha/Fe] \approx +0.3$) are typical of old stellar populations like GCs and elliptical galaxies. The $[\alpha/Fe]$ traces the timescale of star formation activity in galaxies. The majority of α-elements are produced rapidly by Type II supernovae, while Fe is produced by Type Ia SNe on longer timescales. Supersolar $[\alpha/Fe]$ indicates rapid enrichment from Type II supernovae and implies that the galaxy/GC has undergone a short burst of star formation activity. The solar and subsolar abundance ratios indicate slower chemical enrichment or a more quiescent star formation history (van Zee et al. 2004).

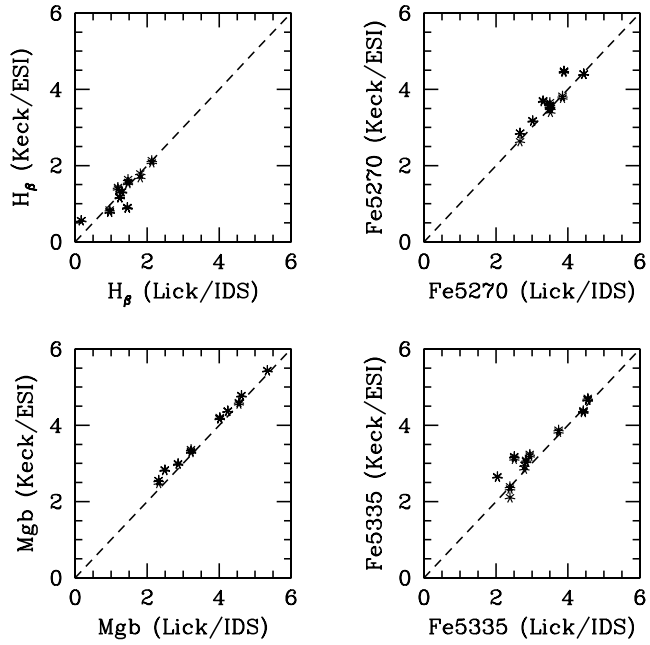

FIG. 7.—Our standard-star index measurements vs. published values from Worthey et al. (1994).

The nuclei of nucleated dwarf ellipticals, taken from Geha et al. (2003), are also shown in the same plot. The majority of the dE nuclei data are consistent with solar $[\alpha/Fe]$ abundance ratios, while the majority of UCDs have supersolar $[\alpha/Fe]$ abundances. This provides evidence that the Virgo UCDs and typical dE,N nuclei are different in that they have different formation histories. Our dE,N (VCC 1407) lies, however, along the UCD relation, together with two dE,Ns from Geha et al. (2003).

In Figure 9 we show the age-sensitive Hβ index versus the metallicity-sensitive [MgFe]′ index ($[MgFe]' = [Mg\,b \times (0.72Fe\,\lambda5270 + 0.28Fe\,\lambda5335)]^{1/2}$) and compare them with the SSP models of Thomas et al. (2003). The [MgFe]′ is largely independent of $[\alpha/Fe]$ and serves best as a tracer of total metallicity (Thomas et al. 2003), and Hβ is less $[\alpha/Fe]$-sensitive than other Lick Balmer line indices (Thomas et al. 2004). As we can see from the plot, *the Virgo UCDs are old (older than 8 Gyr) and have metallicities between* $[Z/H] = -1.35$ *and* +0.35 dex. The SSP models in Figure 9 are shown for the abundance ratio $[\alpha/Fe] = +0.3$. The conclusion about UCD ages and metallicities remains the same if we use $[\alpha/Fe] = 0.0$ and +0.5 models.

As a consistency test, we used the Virgo UCD ages and metallicities derived from Figure 9 and Maraston (2005) SSP models to predict photometric colors and to compare them with the observed ones. The results are summarized in Table 14. The observed colors of Virgo UCDs are in very good agreement with the colors predicted from the derived ages and metallicities.

The ages, metallicities, and abundances of Virgo UCDs are similar to those found for GCs in the galaxies M49 and M87 in the Virgo Cluster by Cohen et al. (2003, 1998). According to Cohen et al. (2003), the M49 GCs have metallicities in the range from $[Z/H] = -1.3$ to +0.5 dex and in mean are older than 10 Gyr. The metallicity and age parameters for M49 and M87 GCs are basically identical. The GC systems of both of these galaxies are α-enhanced by a factor of about 2 above the solar value.

We also find that the Virgo UCDs have older integrated stellar populations on average than the present-day dE,N nuclei.

TABLE 16
THE MEAN OFFSETS BETWEEN OUR INSTRUMENTAL SYSTEM AND THE LICK/IDS SYSTEM

Index	Lick − ESI	rms Scatter	Lick rms per Observation
Hβ (Å)	0.00	0.12	0.22
Mg *b* (Å).....	−0.13	0.05	0.23
Fe λ5270 (Å)	−0.04	0.09	0.28
Fe λ5335 (Å)	−0.08	0.21	0.26

NOTES.—The mean offsets were calculated as average differences between the published index values and our measurements for all observations of nine calibration stars. The outliers (1 or 2 for each index) were excluded. The rms scatter about the mean is also given. The rms uncertainty per observation of the Lick calibrators (Worthey et al. 1994) is given in the last column.

However, we note that UCDs are not distinct from the oldest dE,N nuclei of Geha et al. (2003), and our dE,N, VCC 1407, lies with the UCDs.

The general trend of UCDs to lower metallicities and older ages than the dE nuclei in Figure 9 is not consistent with the naive threshing model in which UCDs are identical to the present-day nuclei of dE galaxies. These results may, however, be consistent with variations of the threshing hypothesis in which the parent objects are disrupted at an early time when star formation is still going on and gas is present (e.g., Mieske et al. 2006). In this scenario, the stripping selectively halts the star formation in the stripped objects (UCDs), giving them lower metallicities and older ages compared to the nuclei which continue to form stars. However, this may not be consistent with the [α/Fe] abundances found in Virgo UCDs: their supersolar abundances imply rapid enrichment in a short burst of star formation. This seems to be inconsistent with gas stripping over an extended period, unless the stripping process caused a very sudden halt to the star formation.

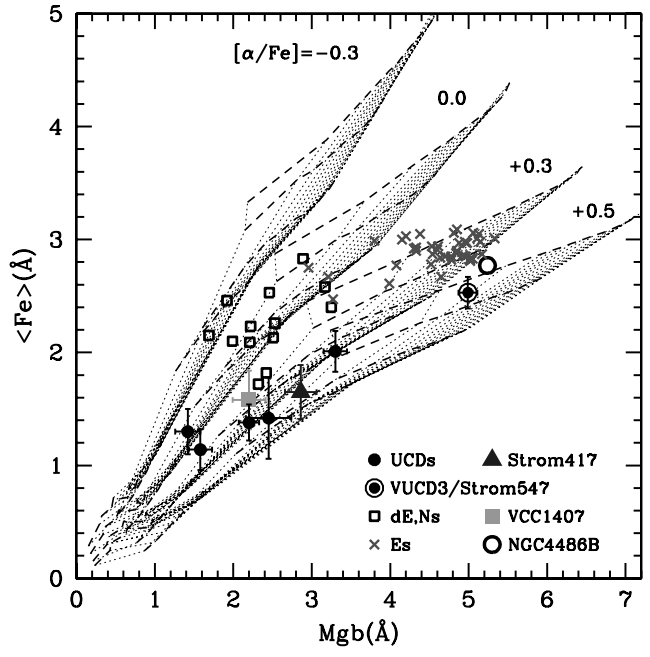

FIG. 8.—Comparison of our data, Mg *b* vs. ⟨Fe⟩, with model grids from Thomas et al. (2003). Open squares represent dE,Ns from Geha et al. (2003). Elliptical galaxies from Trager et al. (2000) are shown with crosses. Other symbols represent our data. Thomas et al. (2003) models with variable [α/Fe] are plotted for ages of 1–15 Gyr in increments of 1 Gyr (*dotted lines, from left to right*) and metallicities of −2.25, −1.35, −0.33, 0.0, +0.35, and +0.67 dex (*dashed lines, from bottom to top*). [*See the electronic edition of the Journal for a color version of this figure.*]

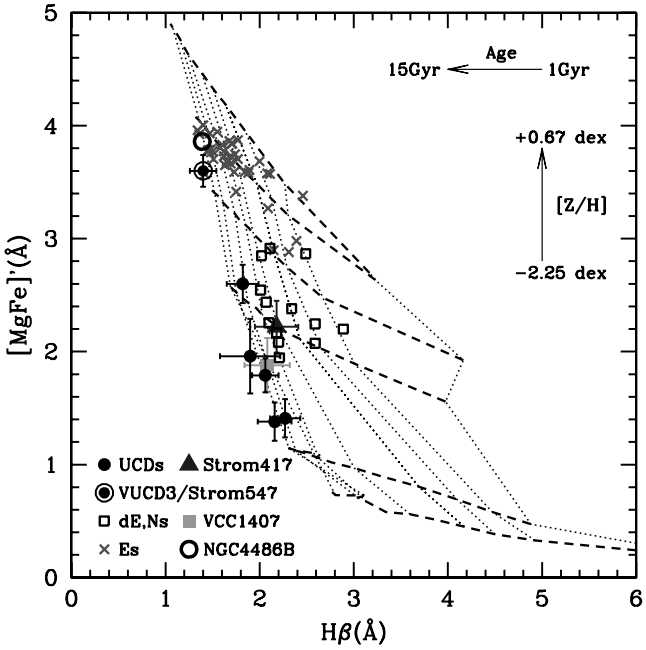

FIG. 9.—Comparison of our data, Hβ vs. [MgFe]′, with model grids from Thomas et al. (2003). Open squares represent dE,Ns from Geha et al. (2003). Elliptical galaxies from Trager et al. (2000) are shown with crosses. Other symbols represent our data. Thomas et al. (2003) models are plotted for ages of 1, 2, 3, 4, 6, 8, 10, 12, and 14 Gyr (*dotted lines, from right to left*), metallicities of −2.25, −1.35, −0.33, 0.0, +0.35, and +0.67 dex (*dashed lines, from bottom to top*), and [α/Fe] = +0.3. [*See the electronic edition of the Journal for a color version of this figure.*]

We also measured the near-infrared Ca II triplet (CaT) index for Virgo UCDs (as defined in Cenarro et al. 2001) to compare it with the metallicity derived from the Lick indices above. SSP models predict a strong dependence of the CaT index on metallicity for subsolar metallicities (Vazdekis et al. 2003; Maraston 2005). GCs are found to follow the model predictions very well for metallicities typical of Galactic GCs (up to about a solar metallicity; Saglia et al. 2002; Maraston 2005), whereas normal and dwarf elliptical galaxies deviate from SSP model predictions (Saglia et al. 2002; Michielsen et al. 2003). Michielsen et al. (2003) obtained CaT values for a sample of dEs and found that four of five dEs with independent metallicity estimates have CaT ∼ 8 Å, which is much higher than expected from their low metallicities ($-1.5 < [Z/H] < -0.5$). Saglia et al. (2002) found that the CaT values for bright ellipticals (7.3 ± 1.0 Å) are lower than predicted by SSP models for their ages and metallicities ($0.0 < [Z/H] < +0.7$).

The CaT index values for our Virgo objects are listed in Table 17. The uncertainties were calculated based on the noise spectrum of each object. The resolution of the Cenarro et al. (2001) stellar library is very close to our spectral resolution, so no correction for resolution was needed. The measured indices for stars in common with the Cenarro et al. library showed good agreement between our instrumental system and Cenarro et al. system. The CaT index for the NGC 4486B galaxy was corrected for the effects of internal velocity dispersion using a K-type stellar template (see Cenarro et al. 2001).

Figure 10 presents the [*Z*/H] metallicity versus the CaT index for the Virgo UCDs, Strom 417 (a GC), VCC 1407 (a dE,N), and the NGC 4486B galaxy. The metallicities were derived from the Lick indices (Fig. 9). In Figure 10 we also plot Maraston (2005) SSP model predictions with a Salpeter IMF for ages of 4, 9, and 15 Gyr. It is hard to make any strong conclusions from this figure

TABLE 17
CaT Index

Object	CaT (Å)
VUCD 1	7.51 ± 0.32
VUCD 3/Strom 547	6.92 ± 0.27
VUCD 4	5.71 ± 0.45
VUCD 5	7.97 ± 0.35
VUCD 6	6.13 ± 0.41
VUCD 7	6.37 ± 0.71
Strom 417	8.62 ± 0.45
VCC 1407	6.90 ± 0.51
NGC 4486B	7.32 ± 0.09

due to the large uncertainties in the data, but it appears that for subsolar metallicities the Virgo UCDs and Strom 417 follow the SSP model predictions (within the uncertainties). VUCD 3 deviates strongly from the model predictions. It has a supersolar metallicity and lies in the plot with NGC 4486B and other Es from Saglia et al. (2002). There are no CaT data for GCs at these metallicities available in the literature yet, so we cannot conclude whether VUCD 3 is globular-like or not. Our dE,N (VCC 1407) lies with the UCDs in the [Z/H] versus. CaT plot. The CaT value for VCC 1407 is consistent with the SSP model predictions (within the uncertainties). However, as we already mentioned above, one of the five dEs studied by Michielsen et al. (2003) also has a CaT in agreement with the model predictions for its metallicity, but all the rest do not. Given that GCs are known to follow SSP model predictions (for subsolar metallicities), whereas dE and E galaxies do not (Saglia et al. 2002; Michielsen et al. 2003), then Figure 10 suggests that the Virgo UCDs have CaT indices more like GCs than galaxies.

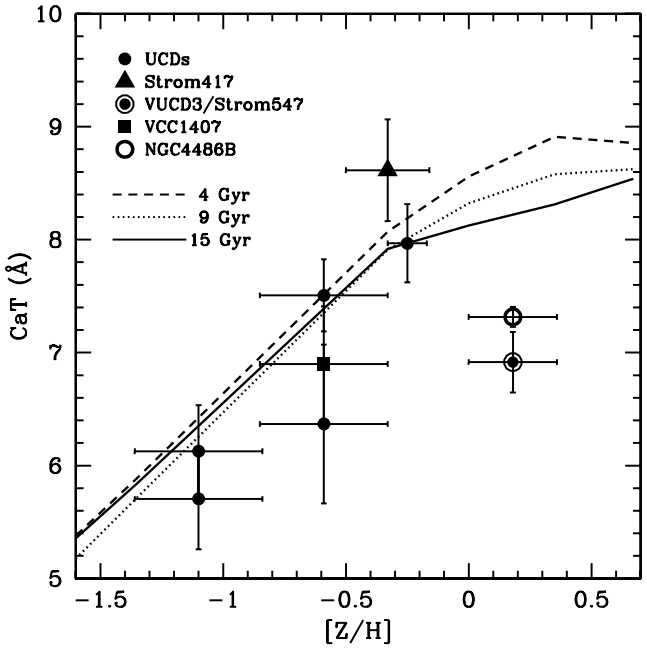

Fig. 10.—Comparison of our data, metallicity vs. CaT index, with Maraston (2005) SSP model predictions (Salpeter IMF). The SSP models are plotted for ages of 4, 9, and 15 Gyr.

7. SUMMARY AND CONCLUSIONS

In this paper we have presented new imaging and spectroscopic observations of six Virgo Cluster UCDs (discovery reported by Jones et al. 2006), along with reanalyzed data for five Fornax Cluster UCDs (initially presented by Drinkwater et al. 2003). These are the most luminous UCDs: $-14 < M_V < -12$. The main results of our analysis of these data are as follows:

1. From *HST* imaging we find that most of the UCDs have shallow or steep cusps in their cores; only one UCD has a flat "King" core. We also find that none of the UCDs show tidal cutoffs down to our limiting surface brightness. These properties are not consistent with the standard King models with flat cores and tidal cutoffs used for most GCs. However, recent work has shown that GCs can have such parameters. Noyola & Gebhardt (2003) obtained inner logarithmic slopes of profiles for 28 Galactic GCs and found that the slopes span a continuous range from zero to 0.6, featuring central cusps as well as flat King cores. It is known that young GCs can have extended halos (e.g., Elson et al. 1987), but McLaughlin & van der Marel (2005) have now shown that extended halos are a generic characteristic of massive GCs—both young and old—in the Magellanic Clouds.

2. Fundamental plane projections reveal (1) that Virgo UCDs have properties similar to those of Fornax UCDs and (2) that the UCDs and transition objects of Haşegan et al. (2005) appear to follow the same relation between luminosity and velocity dispersion as old GCs.

In the κ_1-κ_3 plane the UCDs lie on the same tight correlation between mass and M/L ratio as the bright GCs and transition objects of Haşegan et al. (2005), but the fainter GCs ($\kappa_1 < 0$) show little if any correlation in this plane. This corresponds to a mass of $\approx 10^6\,M_\odot$, at which Haşegan et al. (2005) find a turnover in scaling relations for low-mass systems in other projections of the fundamental plane.

In the κ_1-κ_2 plane the UCDs are not on the main GC relation as defined by the MW and M31 GCs, but the available data do not provide any evidence for a gap between UCDs and GCs in this plane.

The dE,N nuclei in the Virgo Cluster with similar masses/luminosities to the UCDs lie in the same region of all fundamental plane projections as the UCDs. This is consistent with the threshing hypothesis for UCD formation from early-type dwarf galaxies by the removal of low surface brightness envelope.

3. The age and metallicity analysis shows that Virgo UCDs are old (older than 8 Gyr) and have metallicities ranging from [Z/H] $= -1.35$ to +0.35 dex.

The observed colors of Virgo UCDs are in agreement with the colors predicted from the derived ages and metallicities.

Five UCDs and Strom 417, a GC, have supersolar abundance ratios, $[\alpha/\mathrm{Fe}] \approx +0.3 - +0.5$, and one UCD has a solar abundance ratio, $[\alpha/\mathrm{Fe}] \approx 0.0$. The supersolar $[\alpha/\mathrm{Fe}]$ abundances are typical of old stellar populations found in GCs and elliptical galaxies.

Virgo UCDs and typical present-day dE,N nuclei are different in that they have different $[\alpha/\mathrm{Fe}]$ abundance ratios and, therefore, have different formation histories.

The ages, metallicities, and abundances of Virgo UCDs are similar to those found for GCs in the galaxies M49 and M87 in the Virgo Cluster.

UCDs generally have lower metallicities and older ages than dE nuclei: this is not consistent with the naive threshing model in which UCDs are identical to the present-day nuclei of dE galaxies.

Measurements of the near-IR CaT index suggest that Virgo UCDs have stellar populations more like those found in GCs than in dE and E galaxies.

4. The Virgo and Fornax UCDs all have masses $\approx(2-9)\times 10^7\ M_\odot$ and M/L ratios $\approx(3-5)\ M_\odot/L_{\odot,V}$.

UCDs are more massive than transition objects of Haşegan et al. (2005) and all known GCs for which dynamical mass estimates are available.[8]

Although the UCDs are more massive than known GCs, they are within the theoretical limits for the most massive GCs formed in galaxies as large as M87 and NGC 1399 (see eq. [8] of Kravtsov & Gnedin 2005).[9] Recent simulations (Yahagi & Bekki 2005; Bekki & Yahagi 2006) confirm that GCs can escape the potential of these galaxies.

The UCD masses are close to the estimated masses of some young massive GCs such as NGC 7252:W3, NGC 7252:W30, and NGC 1316:G114 (Maraston et al. 2004; Bastian et al. 2006), whose origin is suggested to be by early mergers of lower mass stellar clusters (Kissler-Patig et al. 2006). As these objects evolve they will lose mass, and their structural parameters will also change (e.g., Fellhauer & Kroupa 2005). It is not clear whether they will still have the same masses (and other parameters) as UCDs after the very long evolution times demanded by our old age estimates for the Virgo UCDs.

The dynamical M/L ratios for Virgo UCDs are consistent with the SSP model predictions (by Maraston 2005) within the uncertainties. It implies that Virgo UCDs do not require dark matter to explain their M/L ratios. This conclusion applies to the central region, where we have velocity dispersion data covered by our spectroscopic observations. An increasing dark matter contribution toward larger radii cannot be ruled out with the present data.

Note that while the structural properties and internal velocity dispersions have been measured for all the UCDs, the ages and metallicities (and the interpretation of the M/L ratios) are limited to the Virgo UCDs for which we have this data. The high-resolution spectra for Fornax UCDs used by Hilker et al. (2007) have too low S/N for the Lick index measurements. Also, no Lick standards were observed for the calibration onto the Lick/IDS system. Mieske et al. (2006) present [Fe/H] metallicities and Hβ indices for 26 compact objects in Fornax, including UCD 2, UCD 3, and UCD 4 and four more objects with luminosities similar to our five Fornax UCDs. The metallicities derived for Virgo UCDs are total metallicities [Z/H]. The [Z/H] and [Fe/H] are related as follows: $[\mathrm{Fe/H}] = [Z/\mathrm{H}] - 0.94[\alpha/\mathrm{Fe}]$ (Thomas et al. 2003). Assuming Fornax and Virgo UCDs have similar mean α-abundances, $[\alpha/\mathrm{Fe}] = +0.3$, the bright Fornax compact objects in Mieske et al. (2006) have mean metallicity $[Z/\mathrm{H}] \approx -0.34$, which is similar to the mean metallicity for Virgo UCDs. The Hβ indices in Mieske et al. (2006) are not calibrated, so no reliable conclusions can be drawn, but the appearance at least is for the Fornax objects to have higher Hβ (2.02–2.86 Å), and hence younger mean ages compared to the Virgo UCDs. This suggests a difference in formation time, if not mechanism, for UCDs in the two galaxy clusters. However, we prefer to refrain from any firm conclusions on Fornax UCD origins until accurate age, metallicity, and α-abundance estimates are obtained for them; these should in turn be compared to the properties of *Fornax Cluster* GCs and dwarf galaxy nuclei. In the following discussion our conclusions focus mainly on the Virgo UCDs.

The common feature in all the above results is that our detailed measurements of the internal UCD properties give values consistent with the observed properties of GCs. In all the parameters we have investigated there is no evidence for any gap between GCs and UCDs. The ages, metallicities, and abundances of the Virgo UCDs are similar to those found for GCs in the two brightest Virgo galaxies (M49 and M87). This suggests that UCDs and GCs could have the same formation epoch and the same star formation history. Theoretical work shows that such massive objects as UCDs could form in M87 and NCG 1399 and subsequently escape the host galaxy potential (Kravtsov & Gnedin 2005; Yahagi & Bekki 2005; Bekki & Yahagi 2006). The surface brightness structure of the UCDs is not different to that of GCs in the MW and Magellanic Clouds. The M/L ratios of the Virgo UCDs are consistent with SSPs as in GCs.

We therefore conclude that the internal properties of Virgo UCDs are consistent with them being the high-mass/high-luminosity extreme of known GC populations.

Some of our results, notably the fundamental plane projections, are consistent with the formation of UCDs by the simple removal of the halo from the nuclei of nucleated dwarf galaxies. However, the ages, metallicities, and abundances for Virgo UCDs are not consistent with this simple stripping model. It might be consistent with more sophisticated models of the stripping process that include the effects of gas removal on the chemical evolution of the nuclei.

As we have shown that the Virgo UCDs are old, we note that definitive tests of theories of their formation by stripping processes or the evolution of merger-formed massive star clusters will need to consider the effects of gas processes (especially gas removal) over these long timescales.

E. A. E. and M. J. D. acknowledge support from the Australian Research Council. M. D. G. gratefully acknowledges support by the National Science Foundation under grant 0407445. Some of the work reported here was done at the Institute of Geophysics and Planetary Physics, under the auspices of the US Department of Energy by Lawrence Livermore National Laboratory under contract W-7405-Eng-48. The authors particularly wish to thank Chien Peng (STScI) for very valuable assistance and discussions concerning the use of his GALFIT software. We also wish to thank Harry Ferguson (STScI) and Anton Koekemoer (STScI) for assistance with the *HST* data analysis, Holger Baumgardt (University of Bonn) for help with the dynamical calculations, and Richard White (STScI) for allowing us to use his ESI reduction scripts, which we then modified for our specific purposes. We are grateful to the referee for very helpful comments and suggestions, which have improved this paper.

This work is based on data obtained at the W. M. Keck Observatory, which is operated as a scientific partnership among the California Institute of Technology, the University of California, and the National Aeronautics and Space Administration. The Observatory was made possible by the generous financial support of the W. M. Keck Foundation.

[8] The systems with dynamical masses are G1, $(7-17)\times 10^6\ M_\odot$ (Meylan et al. 2001); ω Cen, $5\times 10^6\ M_\odot$ (Meylan et al. 1995); NGC 5128 GCs, $(1-9)\times 10^6\ M_\odot$ (Martini & Ho 2004); and the transition objects of Haşegan et al. (2005), $(0.5-2.5)\times 10^7\ M_\odot$.

[9] The mass of M87 within 32 kpc is $(2.4\pm 0.6)\times 10^{12}\ M_\odot$ according to Wu & Tremaine (2006), and the mass of NGC 1399 within 50 kpc is $\approx 2.0\times 10^{12}\ M_\odot$ as found by Richtler et al. (2004).

REFERENCES

Barmby, P., Holland, S., & Huchra, J. P. 2002, AJ, 123, 1937
Bastian, N., Saglia, R. P., Goudfrooij, P., Kissler-Patig, M., Maraston, C., Schweizer, F., & Zoccali, M. 2006, A&A, 448, 881
Bekki, K., Couch, W. J., & Drinkwater, M. J. 2001, ApJ, 552, L105
Bekki, K., Couch, W. J., Drinkwater, M. J., & Shioya, Y. 2003, MNRAS, 344, 399
Bekki, K., & Yahagi, H. 2006, MNRAS, 372, 1019
Bender, R., Burstein, D., & Faber, S. M. 1992, ApJ, 399, 462
Bruzual, G., & Charlot, S. 2003, MNRAS, 344, 1000
Burstein, D., Bender, R., Faber, S. M., & Nolthenius, R. 1997, AJ, 114, 1365
Cardiel, N., Gorgas, J., Cenarro, A. J., & González, J. J. 1998, A&AS, 127, 597
Cenarro, A. J., Cardiel, N., Gorgas, J., Peletier, R. F., Vazdekis, A., & Prada, F. 2001, MNRAS, 326, 959
Choi, P. I., Guhathakurta, P., & Johnston, K. V. 2002, AJ, 124, 310
Cohen, J. G., Blakeslee, J. P., & Côté, P. 2003, ApJ, 592, 866
Cohen, J. G., Blakeslee, J. P., & Ryzhov, A. 1998, ApJ, 496, 808
Cottrell, P. L., & Sneden, C. 1986, A&A, 161, 314
Davies, R. L., Sadler, E. M., & Peletier, R. F. 1993, MNRAS, 262, 650
Djorgovski, S. G., Gal, R. R., McCarthy, J. K., Cohen, J. G., de Carvalho, R. R., Meylan, G., Bendinelly, O., & Parmeggiani, G. 1997, ApJ, 474, L19
Drinkwater, M. J., Gregg, M. D., Couch, W. J., Ferguson, H. C., Hilker, M., Jones, J. B., Karick, A., & Phillipps, S. 2004, Publ. Astron. Soc. Australia, 21, 375
Drinkwater, M. J., Gregg, M. D., Hilker, M., Bekki, K., Couch, W. J., Ferguson, H. C., Jones, J. B., & Phillipps, S. 2003, Nature, 423, 519
Drinkwater, M. J., Jones, J. B., Gregg, M. D., & Phillipps, S. 2000, Publ. Astron. Soc. Australia, 17, 227
Elson, R. A. W., Fall, S. M., & Freeman, K. C. 1987, ApJ, 323, 54
Faber, S. M., Wegner, G., Burstein, D., Davies, R. L., Dressler, A., Lynden-Bell, D., & Terlevich, R. J. 1989, ApJS, 69, 763
Fellhauer, M., & Kroupa, P. 2002, MNRAS, 330, 642
———. 2005, MNRAS, 359, 223
———. 2006, MNRAS, 367, 1577
Freedman, W. L., et al. 2001, ApJ, 553, 47
Geha, M., Guhathakurta, P., & van der Marel, R. P. 2002, AJ, 124, 3073
———. 2003, AJ, 126, 1794
Gregg, M. D., & Minniti, D. 1997, PASP, 109, 1062
Hanes, D. A., Côté, P., Bridges, T. J., McLaughlin, D. E., Geisler, D., Harris, G. L. H., Hesser, J. E., & Lee, M. G. 2001, ApJ, 559, 812
Harris, W. E. 1996, AJ, 112, 1487
Harris, W. E., Harris, G. L. H., Holland, S. T., & McLaughlin, D. E. 2002, AJ, 124, 1435
Haşegan, M., et al. 2005, ApJ, 627, 203
Hilker, M., Baumgardt, H., Infante, L., Drinkwater, M., Evstigneeva, E., & Gregg, M. 2007, A&A, 463, 119
Hilker, M., Infante, L., Vieira, G., Kissler-Patig, M., & Richtler, T. 1999, A&AS, 134, 75
Jones, J. B., et al. 2006, AJ, 131, 312
Karick, A. M., Drinkwater, M. J., & Gregg, M. D. 2003, MNRAS, 344, 188
King, I. R. 1966, AJ, 71, 64
Kissler-Patig, M., Jordán, A., & Bastian, N. 2006, A&A, 448, 1031
Kravtsov, A. V., & Gnedin, O. Y. 2005, ApJ, 623, 650
Lauer, T. R., et al. 1995, AJ, 110, 2622
Luck, R. E., & Challener, S. L. 1995, AJ, 110, 2968
Maraston, C. 2005, MNRAS, 362, 799
Maraston, C., Bastian, N., Saglia, R. P., Kissler-Patig, M., Schweizer, F., & Goudfrooij, P. 2004, A&A, 416, 467
Martini, P., & Ho, L. C. 2004, ApJ, 610, 233
McLaughlin, D. E., & van der Marel, R. P. 2005, ApJS, 161, 304
McWilliam, A. 1990, ApJS, 74, 1075
Meylan, G., Mayor, M., Duquennoy, A., & Dubath, P. 1995, A&A, 303, 761
Meylan, G., Sarajedini, A., Jablonka, P., Djorgovski, S. G., Bridges, T., & Rich, R. M. 2001, AJ, 122, 830
Michielsen, D., de Rijcke, S., Dejonghe, H., Zeilinger, W. W., & Hau, G. K. T. 2003, ApJ, 597, L21
Mieske, S., Hilker, M., & Infante, L. 2002, A&A, 383, 823
Mieske, S., Hilker, M., Infante, L., & Jordán, A. 2006, AJ, 131, 2442
Mieske, S., et al. 2004, AJ, 128, 1529
Mihalas, D., & Binney, J. 1981, Galactic Astronomy (San Francisco: Freeman)
Minniti, D., Kissler-Patig, M., Goudfrooij, P., & Meylan, G. 1998, AJ, 115, 121
Noyola, E., & Gebhardt. K. 2003, Rev. Mex. AA Ser. Conf., 18, 78
Peng, C. Y., Ho, L. C., Impey, C. D., & Rix, H.-W. 2002, AJ, 124, 266
Peterson, R. C. 1978, ApJ, 224, 595
Peterson, R. C., & King, I. R. 1975, AJ, 80, 427
Phillipps, S., Drinkwater, M. J., Gregg, M. D., & Jones, J. B. 2001, ApJ, 560, 201
Richtler, T., et al. 2004, AJ, 127, 2094
Saglia, R. P., Maraston, C., Thomas, D., Bender, R., & Colless, M. 2002, ApJ, 579, L13
Schlegel, D. J., Finkbeiner, D. P., & Davis, M. 1998, ApJ, 500, 525
Sirianni, M., et al. 2005, PASP, 117, 1049
Spitzer, L. 1987, Dynamical Evolution of Globular Clusters (Princeton: Princeton Univ. Press)
Strom, S. E., Forte, J. C., Harris, W. E., Strom, K. E., Wells, D. C., & Smith, M. G. 1981, ApJ, 245, 416
Thomas, D., Maraston, C., & Bender, R. 2003, MNRAS, 339, 897
Thomas, D., Maraston, C., & Korn, A. 2004, MNRAS, 351, L19
Tonry, J., & Davis, M. 1979, AJ, 84, 1511
Trager, S. C., Faber, S. M., Worthey, G., & González, J. J. 2000, AJ, 119, 1645
Queloz, D., Dubath, P., & Pasquini, L. 1995, A&A, 300, 31
Valdes, F., Gupta, R., Rose, J. A., Singh, H. P., & Bell, D. J. 2004, ApJS, 152, 251
Vazdekis, A., Cenarro, A. J., Gorgas, J., Cardiel, N., & Peletier, R. F. 2003, MNRAS, 340, 1317
Worthey, G., Faber, S. M., González, J. J., & Burstein, D. 1994, ApJS, 94, 687
Wu, X., & Tremaine, S. 2006, ApJ, 643, 210
Yahagi, H., & Bekki, K. 2005, MNRAS, 364, L86
van der Marel, R. P. 1994, MNRAS, 270, 271
van Zee, L., Barton, E. J., & Skillman, E. D. 2004, AJ, 128, 2797